2015

Novel Optical Applications Based on Photon-phonon Interactions

Ruolin Chen
Lehigh University

Novel Optical Applications Based On

Photon-phonon Interactions

By

Ruolin Chen

Presented to the Graduate and Research Committee

of Lehigh University

in Candidacy for the Degree of

Doctor of Philosophy

In

Electrical Engineering

Lehigh University

August 2015

This dissertation is approved and recommended for acceptance as a dissertation in partial fulfillment of the requirements for the degree of Doctor of Philosophy in Electrical Engineering.

_____

Date

_____

Accepted Date

Committee Members:

_____	_____
Dr. Yujie J. Ding (Advisor and Chair)	Date
_____	_____
Dr. Filbert J. Bartoli	Date
_____	_____
Dr. Nelson Tansu	Date
_____	_____
Dr. Sushil Kumar	Date
_____	_____
Dr. Dimitrios Vavylonis	Date

Acknowledgements

A career in technology has been a long planted seed in my mind, thanks to the unintentional influence from my family: my father, a physics professor, used to take me to his lab when I was little, letting me play with the retired experimental instrument; my mother had been an engineer in a chemical factory for her early career; my grandparents on my mom's side, both worked in a hospital before they retired, as a dentist and a nurse. They never forced me to learn anything about math or physics or chemistry or medicine. However, it seems so natural to me that I gradually developed my thinking to at least ask "how" and a lot of times, "why" things would happen or work in their certain ways. After obtaining a bachelor of science in physics, I realized that the law of physics, though beautiful in many ways, cannot make sense to me if it is not applied to things in real life. It was the perfect timing that an offer from Prof. Yujie Ding at Lehigh University came to my dorm in Shanghai, and the journey of my PhD in Electrical Engineering began 5 months afterwards.

Getting a PhD was never easy. There were good days and bad days, happiness when finally the experiment worked, frustrations when nothing exciting was going on, fatigue after an all nighter of lab work, and the joyfulness when seeing my paper got published. Thankfully to all the great people I met at Lehigh, I was able to finish this journey with brightness and hopefulness in my mind.

I would like to express my deepest appreciation firstly to my advisor, Prof. Ding. He is a knowledgeable professor and thoughtful mentor. His thorough understanding of theories and tremendous ability of mathematical analysis and estimation were always helpful to

breakdown problems into small pieces. He taught me a lot about the ways of thinking, the techniques of experiments, and the art of technical writings. I am especially thankful to him that he gave me plenty of time of space to explore my own interest in science and engineering, so that I could read a lot of books and papers and built up my own understanding. He was also very dedicated to his work. I was lucky to have full support during all of my PhD years so that I can focus on the work and not worrying about food and bills. Academics aside, he was also a helpful and trustworthy friend. He helped many times with my personal difficulties without reluctance. He was also a great conversation companion that we could share our interest in movies and music. All in all, without his guidance, support, and company, I would never be able to finish my PhD.

I would also like to dedicate this paragraph to my appreciations on my committee members. Prof. Bartoli, it was my fortune and honor to meet you in Shanghai for the interview. Thank you for recruiting me to Lehigh, for recommending me to Prof. Ding, and for all your support during all these years. Prof. Kumar, thank you for carrying me on in the last year of my PhD and made sure I met all the deadlines and regulations, and also your help in my dissertation writing. Prof. Tansu, thank you for providing a lot of samples for our lab, they were very helpful to my research. Prof. Vavylonis, thank you for your supports and inputs in my general exams, my dissertation, and my defense.

My research can never be completed with all the collaborations and supports from the great colleagues in our lab. Dr. Guan Sun, it was a great pleasure working with you. Thank you for sharing with me your ideas, for all the discussions we had to help my understanding, for the late nights of experiments we had, and for the revision and inputs in my papers. Also, thank you for the great friendship we shared with all the pool games and

conversations. Dr. Guibao Xu, thank you for teaching me all the experimental techniques and all the logistics in the lab, and thank you for establishing the maintenance of instrument in the lab. Dr. Pu Zhao, thank you for picking me up at ABE airport on my first night in the United States, and also for setting up a great example of doctoral graduate. Dr. Da Li, thank you for all the helps in experiments and all the insightful discussions, and also for all the card games and pot luck dinners we had. Pengda Hong, thank you for all your support and companionship in my hard days. Xiaomu Lin, thank you for being a responsible roommate, a great friend, and an inspiring figure. It is impossible to individually express my appreciations to all of you, so a big thank you to all of you including Dr. Yi Jiang, Dr. Lei Wang, Dr. Zhaojun Liu, Dr. Srinivas Ragam, Dr. Xingquan Zou, Dr. Fengqin Liu, Ran Wang, Zhongyang Li, and Liang Gao.

My life in Lehigh can never be this fruitful without all the amazing friends I met here: Dr. Haosu Tang and Weikai Yin, thank you for being my trustworthy and helpful roommates for 3 years. Ye Wei, thank you for being a great friend, for all the times we shared, and for teaching me to look life from another perspective. Jing Liu, thank you for reminding me to be a better myself every day. A big thank you to all of you including Yuan Wang, Dr. Yi Hu, Dr. Jingyu Wang, Sudeep Khanal, Chongzhao Wu, Yilin Chen, Yiming Tan, James Patounas, Yash Marathe, Jieli Tian, Jiajun Duan, Wenjun Ye, Jialu Li, Han Gao, Jifu Tan, Shunqiang Wang, Dr. Bu Wang, Dan Li, Haoxue Song, Ruolei Han, Yunfei Song, Yang Dong, Wei Luo, and many others I cannot keep on naming without many pages. Thank you for sharing my life.

I would also like to express my thankfulness to my friends, Haiyuan Cao, Dr. Guannan Chen, Wujiong Sun, Dr. Han Liu, Dr. Renhu Ma, Shuangping Liu, Zhe Liu, Dai Tian,

Tianyi Zhang, Jingya Zhang, Kun Ma, thank you for always being there for me in my darkest moments, and thank you for reminding me the happiness and dreams in life.

At last, I would like to thank my parents, for raising me up, for all the supports along the way, and for setting up great examples for me as what a great person should be. Thank you, Dr. Ziyu Chen and Xiaoli Zhu.

Table of Content

List of Tables

List of Figures

Abstract

The phenomena of photon-phonon interactions can be found in all forms of matters including gases, plasma, liquids and solids. The applications based on such interactions, including Raman scattering, Bragg Scattering, polariton resonance, phonon-assisted Antistoke photoluminescence, etc. has been intensively investigated. In this dissertation, we present our study of three novel applications in the field of THz generation, hot phonons in transistors, and optical refrigeration.

In Chapter 1, we studied the backward propagating Terahertz (THz) generation using optical rectification in periodically poled $LiNbO_3$ and $LiTaO_3$ samples with ultrafast laser pulse excitation. With the $LiNbO_3$ sample, we have generated the highest frequency at 4.8 THz at the poling period of 7.1 μm, corresponding to an output wavelength of 62.5 μm. We have observed an enhancement factor as large as 61 in the output power comparing to that generated from bulk $LiNbO_3$, which was attributed to the phonon polariton resonance-enhanced nonlinear optical coefficients. For the $LiTaO_3$ samples, we have reached the highest output power of nearly 100 μW. Based on our study, the effective second-order nonlinear coefficient of $LiTaO_3$ are enhance by factors of from 3.7 to 23, leading to the enhancement of THz output powers. The enhancement is rooted in a polariton resonance at the frequency of 127 cm-1, which can be induced by the nonlinear mixing of two transverse-optical phonons due to strong anharmonicity of $LiTaO_3$. We also designed a second wafer with significantly shorter poling periods, and indeed we have observed the entire resonant peak.

In Chapter 2, we studied the hot phonon behavior of GaN high electron mobility transistors (HEMT). We mainly investigated our effort on two methods utilizing Raman scattering to measure the phonon temperature, i.e. the hot phonon population of GaN HEMT device under operation. The ultimate goal was to employ these methods on the study of isotope disorder introduced GaN device and verify whether its phonon behavior is optimized than that in normal devices. The first method extracts phonon temperatures from the ratio of Antistokes and Stokes Raman signal intensities, which requires complex experimental procedures and tendency to wrong temperature deductions. The second method is based on the fitting of phonon temperature to the shift of Stokes Raman peak model, which leads to simple and fast measurement while sophisticated analysis with strong dependence to sample material properties. Comparing two methods, we believe the second one is advantageous due to our limited experimental condition, and it can be improved with proper calibration of the model.

In Chapter 3, we stuied the upconverstion of photoluminescence (PL) from both a free-standing bulk GaN sample and a GaN nanowire sample. When the excitation energy is in the tail of bandgap edge, the PL upconverstion can be attributed to phonon-assisted Antistokes photoluminescence (ASPL). We explored the potential of laser cooling based on such a phenomena with the analysis of PL intensity trending with pump power, excitation wavelength, and temperature. Such analysis proves the fact that the ASPL we measured is originated in single photon process assisted by phonons.

Chapter 0 Introduction to Photon-phonon Interactions

In the macroscopic world, light-matter interactions are treated in the continuous way, which are described in geometric optics and wave optics in theory. The success of these theories depends on the fact that the wavelength/frequency of light doesn't change during the interactions, since the intensity of light is not strong enough to excite interactions to have exchange of energies with matters. While in the microscopic world, light and matters interact with each other not in a continuous way, but in a quantized manner, i.e. the exchanging of energies and/or momentums in sequences of small portions, which cannot be further scaled down. In occasions that we need to solve problem using the quantized fashion, physicist tends to invent "particles" representing the smallest portions of energies/momentums, hence the terms like photons, phonons, polaritons, exitons, etc. , are invented. Photons represent the smallest portions of optical/electromagnetic energies or momentums at their corresponding wavelengths, whereas phonons represent the smallest portions of lattice vibration energies or momentums at their corresponding frequencies. The relations between their energies E/momentums p and their wavelengths λ/frequencies ω can be written as

$$E = hc/\lambda = \hbar\omega, p = h/\lambda = \hbar\omega/c$$

There are many kinds of photon-phonon interactions. Physicists have been investigating on these interactions intensively, and many useful applications have been developed accordingly. For example, in ferroelectrics like $LiNbO_3$ and $LiTaO_3$, we can utilize their phonon polaritons, which are quasi-particles representing coupling between electromagnetic waves and ions, with their frequencies lying in Terahertz (THz) region to

form resonance with THz waves and enhance their generation output [0.1-0.4]. Another good example is the molecule detection in food and drugs employing techniques of Raman shifts, which are interactions of laser beams and optical phonons. Raman Scattering can also be used to measure temperatures in microelectronic devices [0.5~0.9]. Recently, scientists also discovered that Phonon Assisted Anti-stokes Photoluminescence can be used for cooling down materials/devices [0.10-0.12]. Such application would be extremely applicable if it can be developed to feasibility in semiconductor. The aforementioned photon-phonon interactions all involved optical phonons, which are only excited while intensive light incident is present, typically a laser. These interactions also involves change of photon energies, since the energies of optical phonons are large enough to be non-negligible comparing to ones of photons. Other applications inspired by photon-phonon interactions include jet noise studies and fiber loss studies by utilizing theories of Rayleigh Scattering, which are interactions between light and small energy random acoustic phonons in air, liquid or solids, usually accompany with density variations in certain media; and elastic behavior measurement by formulas of Brillouin Scattering, which are optical responses on small energy acoustic phonons with patterned behaviors; and acoustic optical modulators like Q-Switches in high frequency ultrafast lasers by principles of Bragg Scattering, which are collisions between photons and large energy acoustic phonons. In the process when photons are interacting with acoustic phonons, their energies can be treated as unchanged, since the energies of acoustic phonons are much smaller than ones of photons.

There are still many other kinds of photon-phonon interactions and their corresponding applications cannot be explained in detail in this introduction. Specifically, I would like to

cover three applications induced by photon-phonon interactions in the following of this dissertation:

1. THz Generation Enhancement by Phonon Polariton Resonance
2. Device Thermal Management by Raman Scattering
3. Optical Refrigeration by Phonon Assisted Photoluminescence

Chapter 1 THz Generation Enhanced by Phonon Polariton Resonance

I. Introduction to THz Technology

THz waves are electromagnetic radiations with their frequencies lying in between the microwave and infrared regions of the spectrum, typically in the frequency range of 0.1 THz to 10 THz [1.1], corresponding to the wavelength range of approximately 3,000 μm to 30 μm, see Figure 1. Historically, they have also been recognized in terms such like "far-infrared radiations" or "sub-millimeter waves". The most mature fields of studies of THz waves can be attributed to either the THz spectrum of black body radiations from other galaxies, or analytical theories based on the derivations of Maxwell Equations. However, the technical difficulties of making efficient and compact THz sources and detectors have always been baffling scientists and engineers, resulting in the fact that this part of radiations are left as the "last piece of puzzle" of the whole electromagnetic spectrum. Hence, for the lack of suitable technologies, the academics have attributed THz band the name of "THz Gap".

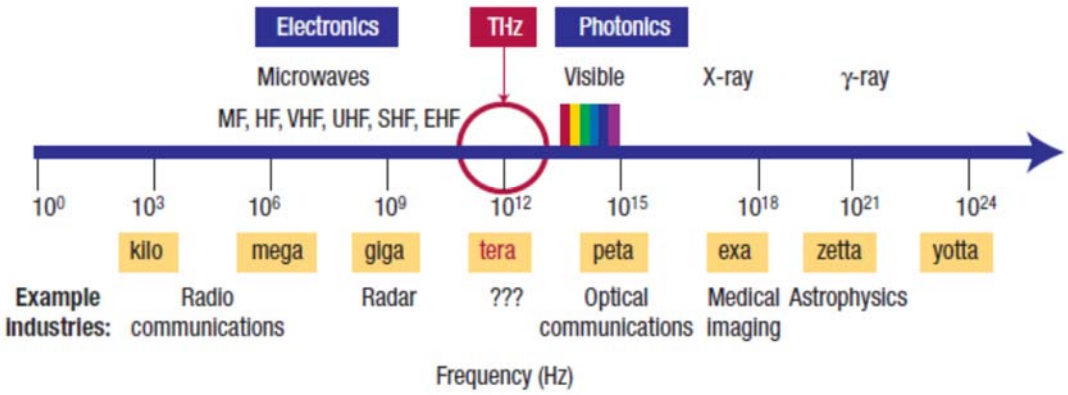

Figure 1.1 The electromagnetic spectrum indicating the THz Gap

Thanks to the development and innovation in photonics, electronics and nanotechnology, the THz Gap has been rapidly vanishing over the past two decades, enabling THz research to be performed in numbers of areas. The current THz technologies have shown promising applications in areas such as biological and medical sciences, non-destructive evaluation, homeland security, information and communications technology (ICT), quality control of food and agricultural products, global environmental monitoring, and ultrafast computing, among many others [1.2].

Today, scientists and engineers have developed many kinds of THz sources. The mechanisms involved in THz generation involves many technologies from electronics to optics, such like optical rectification, difference frequency generation (DFG), quantum cascade lasers (QCLs), photoconducting antennas, build-in field semiconductors, photo demper effect, and plasma among others. According to requirements in potential applications, these sources can be roughly categorized into two by their wave characters: broadband and narrowband. In current academics, broadband THz waves are mostly generated by photoconductive antennas [1.3] using semiconductors like InAs, GaAs, and InP, or DFG using nonlinear optical crystals like $LiNbO_3$ [1.4], $LiTaO_3$, and potassium titanyl phosphate (KTP), whereas narrowband THz waves are provided by laser sources employing quantum cascading technology, based on GaAs/AlGaAs heterostructures, or by backward optical rectification using electro-optical crystals. The difficulties of broadband THz sources mainly lie in their lack of output efficiency for satisfying amount of applicable power. While for QCLs, the requirement of cryogenic cooling limits their feasibility in economic power supply and compactness [1.5, 1.6]. Thus, both categories of THz sources still require further research and development.

In this chapter of the dissertation, I will briefly discuss the studying narrowband THz sources enabled by optical rectification in $LiNbO_3$ and $LiTaO_3$. The high power THz generated through strong absorption are explained by the mechanism of phonon polariton resonance.

II. Phonon Polariton Resonance for THz Generation Enhancement

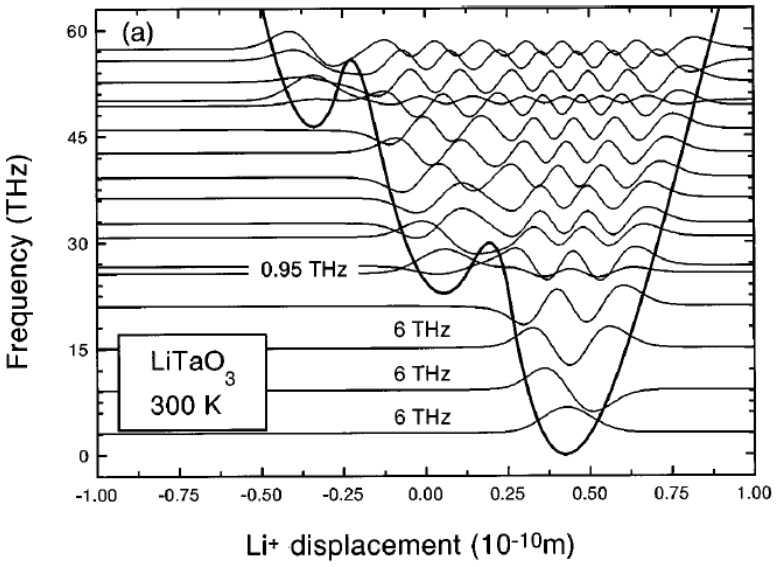

Figure 1.2 Energy-band structure and wavefunctions of optical phonons of $LiTaO_3$. Cited from Ref. [1.7].

Polaritons are quasi-particles defined on the strong coupling of electromagnetic waves with an electronic or magnetic dipole-carrying exitation. Since there are many types of dipoles exist in solid-state materials, polartions are named after the dipole compositions, such like “exiton polaritons”, “phonon polaritons”, “intersubband polaritons”, and “surface plasmon polaritons”. In the special case of phonon polaritons, the coupling is formed between electromagnetic waves and optical phonons, by which the lattice of insulators

composited with positive and negative ions is quantized represented. Typically, the frequencies of these optical phonons lie in the THz band, thus strong resonance with THz waves can be formed leading to the creation of polaritons. As shown in Figure 1.2 [1.7, 1.8], the energy bands of optical phonons in $LiTaO_3$ is plotted against displacement of Li^+ ions, with phonon wavefuctions indicating their energies residing in the THz range accordingly. Such resonance will extremely enhance the effective nonlinear optical coefficient (NOC) of electro-optical materials like $LiNbO_3$ and $LiTaO_3$, providing great possibilities of developing improved generation of THz waves in the spectrum where ample amount of NOC is fulfilled by the resonance, while its effects on index would not severely diminish the THz output by strong absorption and weak transmittance.

The effect of polariton resonance on NOC can be represented as the following formula using the Lorentz oscillator model

$$d_{\text{eff}} = d_{\text{e}}\left[1 + \sum_j S_{\text{rel},j}\frac{\nu_{0j}^2}{\nu_{0j}^2 - \nu^2 - i\nu\Gamma_{0j}}\right] \qquad (1)$$

Here, d_{eff} is the effective NOC; d_{e} is the electronic part of NOC; $S_{\text{rel},j}$ is the relative oscillator strength of the j^{th} polariton resonance, comparing to the electronic NOC; ν_{0j} is the j^{th} resonance frequency of the polariton; ν is the THz frequency; and Γ_{0j} is the linewidth of the j^{th} polariton resonance results from damping effects. As shown in Figure

1.3 [0.1], two polariton resonances at 16 μm and 40 μm of LN have resulted in enormous NOC enhancement.

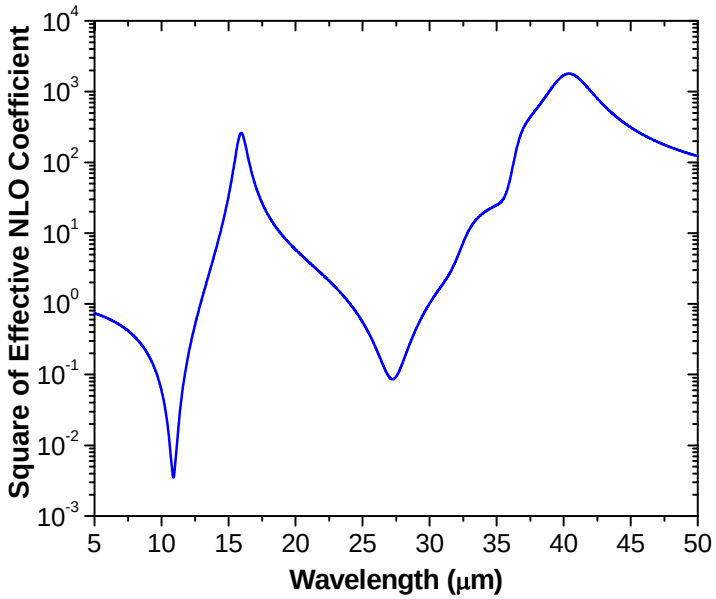

Figure 1.3 The effect of polariton resonance on effective NOC. Cited from Ref. [1.24].

Considering trade-offs between gain and loss, samples of ferroelectric crystals can be designed for the generation of certain THz wavelengths, which will be discussed in the following subsection.

III. THz Generation in $LiNbO_3$ and $LiTaO_3$ through Optical Rectification

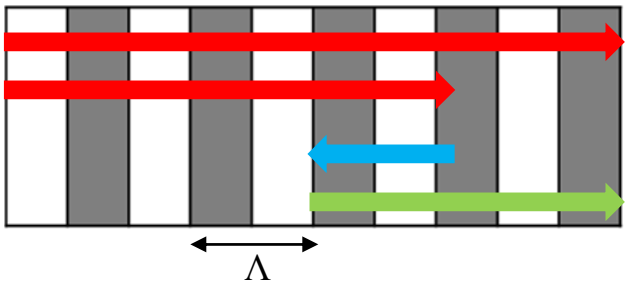

Figure 1.4 Periodic-poled grating of LN or LT for optical rectification

Optical rectification is the reverse process of electro-optic (EO) sampling [1.9], which can be described as jiggling of electric dipoles formed by positive and negative ion pairs. The dipoles are excited by ultrafast laser beams with pulse width in the range of several hundreds of femtoseconds (fs), resulting in the dipole oscillation in THz frequencies, and hence the generation of THz pulses. In nonlinear optics, it can be thought as the difference frequency mixing of two frequencies in the ultrafast laser spectrum, with their difference lying in the THz band. Since the large discrepancy between indices of optical waves and THz waves in nonlinear crystals, the traditional phase-matching cannot be realized in a collinear configuration. In ferroelectric materials like $LiNbO_3$ (LN) and $LiTaO_3$ (LT), their dipoles can be aligned in upward and downward sequences through electric periodic poling (PP), see Figure 1.4 [1.10]. Thus, their largest second order nonlinear optical coefficient (NOC) (for example, the largest NOC of LN lies in the zz direction in the value of d_{33}=27 pm/V) can be applied to parametric generation of THz waves through quasi-phase-matching (QPM). The QPM mechanism takes advantage of the inverse of poling period, and use it to compensate the mismatch between optical and THz wavevectors. The QPM relation can be represented in the following formula [1.10, 1.11, 1.12]

$$k_3 - \frac{2\pi}{\Lambda} = k_2 \pm k_{\mathrm{THz}} \qquad (2).$$

Here, $k_{2,3} = (2\pi/\lambda_{2,3})n_{2,3}$ are the wavevectors of two optical waves coming from the femtosecond laser pulse, with their corresponding wavelengths and indices. $k_{\mathrm{THz}} = (2\pi/\lambda_{\mathrm{THz}})n(\lambda_{\mathrm{THz}})$ is the wavevector of the THz wave. The plus/minus sign indicates forward/backward configuration of THz generation, i.e. the propagation direction

of THz radiation is the same/opposite of that of the excitation laser. After some simplification, the relationship between THz output wavelengths λ_{THz} and poling periods Λ can be written as [1.10, 1.11, 1.12]

$$\lambda_{\mathrm{THz}} = \Lambda[n_{\mathrm{pg}} \mp n(\lambda_{\mathrm{THz}})] \qquad (3).$$

Here, n_{pg} is the group index of the pump ultrafast laser beam, while $n(\lambda_{\mathrm{THz}})$ is the phase index of THz waves in their corresponding wavelengths. The minus/plus sign indicates forward/backward THz generation configuration. The backward configuration has obvious advantages over the forward configuration, including narrow linewidth of generated THz pulse, reaching the optimal interaction region for the optical rectification process, and minimizing the absorption of the THz pulses generated by the nonlinear crystals. As we can see, there is a wavelength choosing mechanism behind this formula. By designing specific poling periods through information of indices and pumping wavelengths, the output wavelength can be accurately pre-selected.

The advantages of our scheme of THz generation is threefold: first, comparing to the forward configuration of optical rectification which mainly generates broadband THz pulses, the backward configuration can be used to generated narrowband THz waves. Due to the extremely large difference of optical and THz wave numbers, the forward configuration allows more possible combinations of quasi-phase-matching relations, results in a broad spectrum of THz output. While in the backward configuration, only one quasi-phase-matching relation is allowed so that a narrowband output can be realized. Second, due to the large absorption induced by polariton resonance, the forward configuration of THz generation experiences extreme power loss. While for the backward configuration, THz waves are able to propagate outside of the material immediately after

each cycle of generation. Third, comparing to THz quantum cascade lasers (QCLs) which also produces narrowband THz but need to operate at cryogenic temperature, our scheme can operate at room temperature, thus eliminating the cost and space occupation of expensive and large cooling facilities.

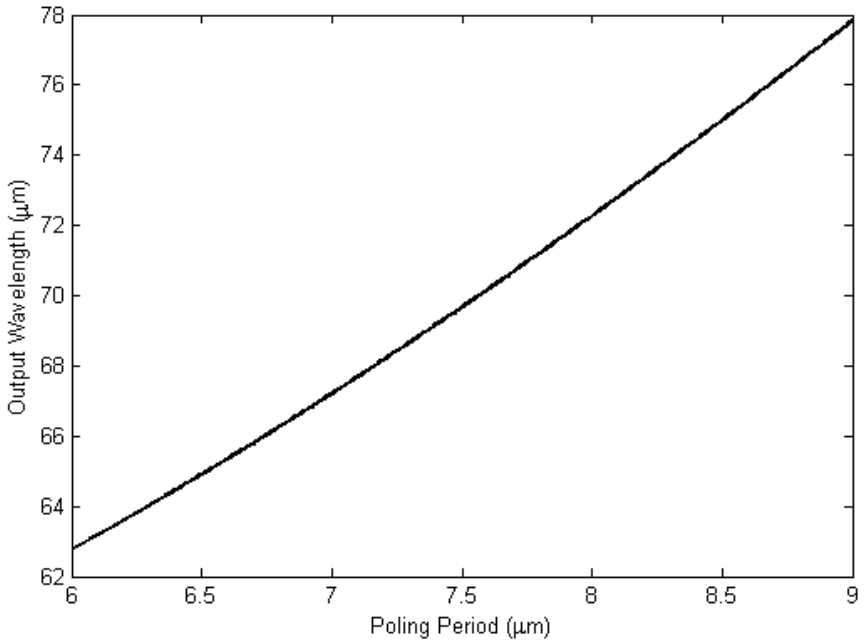

Figure 1.5 Relationship between THz output wavelengths and poling periods

IV. Sample information and Experimental Design

To test the effects of polariton resonance on THz output enhancement, we designed 2 pieces of LN and 2 pieces of LT wafers with theoretical output wavelengths close to certain polariton frequencies. The first piece is a periodic-poled LN (PPLN) wafer containing 6 PP gratings with periods of 6.10 μm, 6.30 μm, 7.10 μm, 7.30 μm, 8.40 μm, 8.60 μm, corresponding to prospective output wavelengths form 63 μm to 76 μm, as shown in Figure 5. This sample is intended for testing the 40 μm resonance of LN polariton [0.3]. The

second piece of PPLN wafer contains 5 PP gratings with periods of 10.0 μm, 10.5 μm, 11.0 μm, 11.5 μm, 12.0 μm, corresponding to the theoretical THz output wavelengths of 79 μm to 94 μm. This sample will be used as a comparison to the PPLT results. The first piece of PPLT wafer contains 8 PP gratings from 10.0 μm to 12.0 μm, with corresponding theoretical output wavelengths from 94 μm to 111.3 μm. Since the effective NOC of LT has not been studied yet, we assumed that its polariton frequencies would not be far from the ones of LN [0.4]. The second piece of PPLT wafer contains 12 PP gratings with periods from7.0 μm to 9.2 μm, corresponding to the theoretical output wavelengths from 78 μm to 84 μm. This wafer will be used to verify our assumption of LT polariton resonance wavelength. A Ti:Sapphire laser amplifier is chosen as the pumping source with an output wavelength of 786 nm, a pulse width of roughly 200 fs, and a repetition frequency of 250 kHz. The backward radiating THz waves would be collected and focused by parabolic mirrors into a bolometer for power measurement. A schematic description of the experimental setup is shown in Figure 1.6.

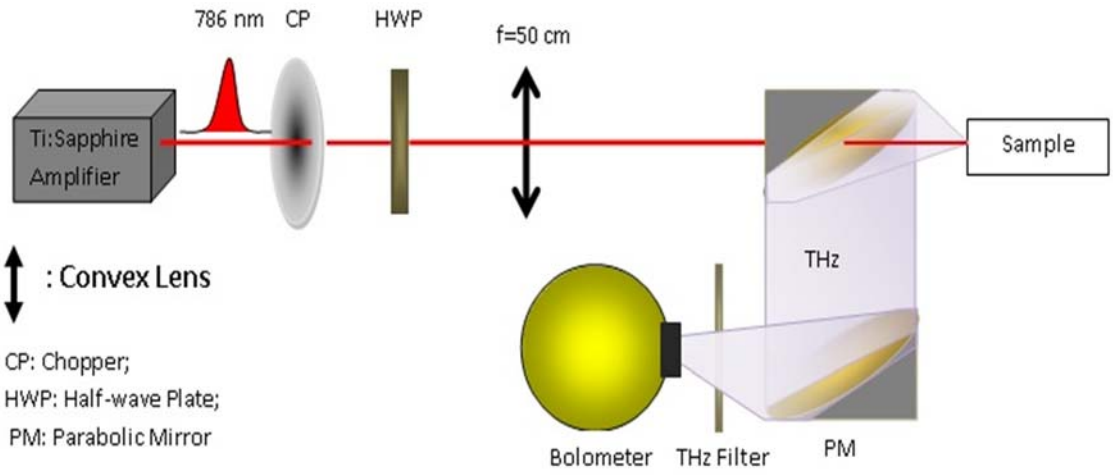

Figure 1.6 Experimental Setup of THz generation

V. THz generation investigations of PPLN

Figure 1.7 shows the spectra for the backward-propagating THz waves generated from the PPLN gratings, measured by rotating a mechanical grating being optimized for the THz frequencies. The grating has a period of 126.7 μm with first-order blazing angle being 26.7°. For the poling periods of 8.60 μm, 8.40 μm,

Table 1.1. Summary of Physical Quantities Measured or Deduced following Investigation of Backward THz Generation from PPLN Wafers.

Grating Number	1	2	3	4	5	6
Poling Period (μm)	6.10	6.30	7.10	7.30	8.40	8.60
Calculated THz Wavelength (μm)	63.18	64.03	67.68	68.66	74.43	75.54
Measured Peak Wavelength (μm)	N/A	N/A	62.5	64.0	70.5	71.5
Effective Interaction Length (μm)	N/A	N/A	13.82	13.89	14.16	14.16
Output Power (nW)	72.63	55.28	110.4	121.0	160.6	201.8

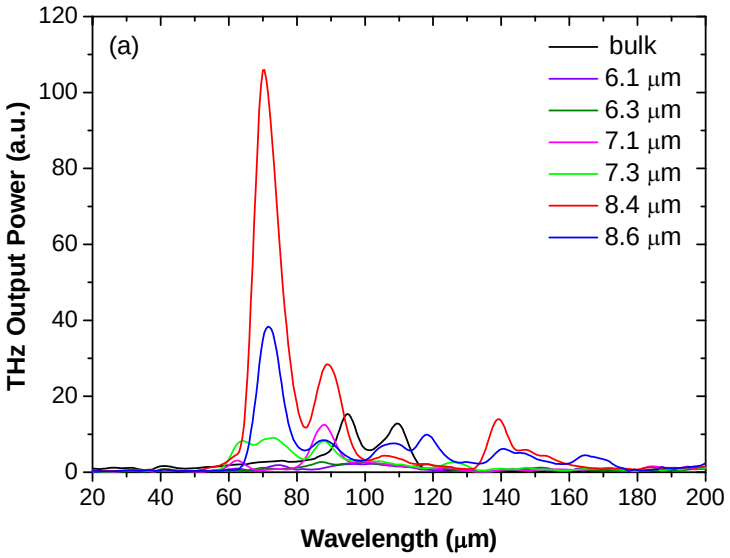

Figure 1.7 Spectrum of THz output power generated by multi-grating PPLN and uniformly poled $LiNbO_3$ (bulk) chips

7.30 μm , and 7.10 μm, clear peaks of THz signals can be identified at the center wavelengths of 71.5 μm, 70.5 μm, 64.0 μm , and 62.5 μm , respectively. The backward-generated THz wavelengths obey the QPM condition described by Eq. (3) with a plus sign. By fitting the available indices of refraction [1.13], we have obtained an empirical expression $n(\lambda_{\mathrm{THZ}}) \approx \sqrt{6.827 + 18.72\lambda_{\mathrm{THZ}}^2/(\lambda_{\mathrm{THZ}}^2 - 2721)}$. It can be shown from Table 1-1 that these four QPM wavelengths are consistent with those calculated by Eq. (3). The slight deviations of the measured values from the calculated ones are most likely caused by the fabrication errors of poling period and the accuracies of THz phase indices calculated using the expression above. These wavelengths are much shorter than those generated by us previously [1.14]. Indeed, in our previous result [1.14], the shortest wavelength was measured to be 126 μm at the poling period of 16.9 μm. In our present work, the shortest wavelength is measured to be about 60 μm at the poling period of 7.1 μm. For the poling periods of 6.10 μm and 6.30 μm,

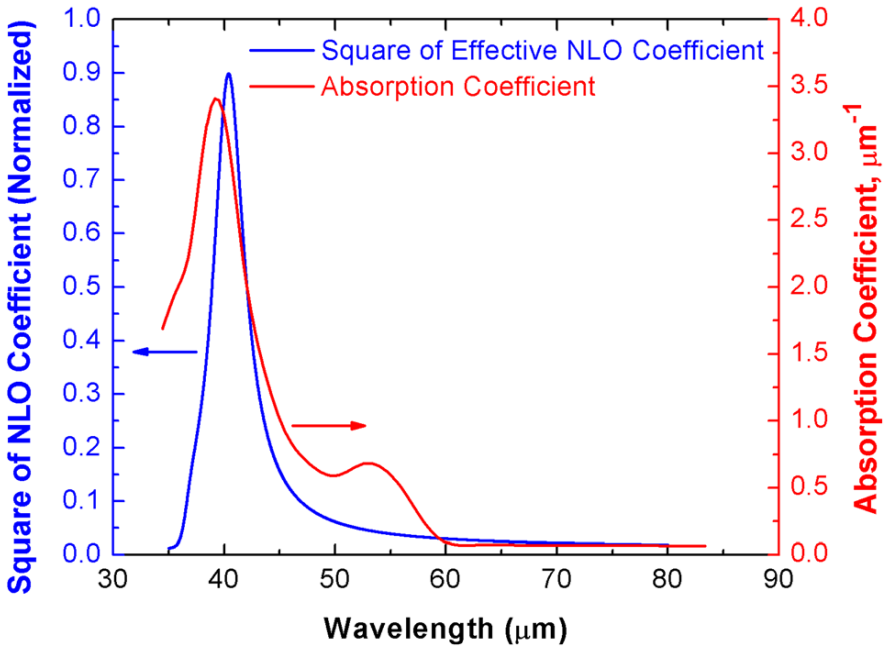

Figure 1.8 Square of effective NLO coefficient normalized by square of electronic NLO coefficient (blue); absorption coefficient is plotted versus wavelength (red).

however, only small modulations have been observed compared with the spectrum measured on a uniformly-poled $LiNbO_3$ crystal. There are three factors limiting the strength of the peak on the short-wavelength side. First, our pump laser has a limited bandwidth of 11.4 nm, which limits the shortest THz wavelength to be about 54 μm. Second, the polariton resonance centered at 40 μm plays the fundamental limit for the backward THz signals due to strong absorption. We have plotted the absorption coefficient of $LiNbO_3$ in the region centered at 40 μm, see Figure 8. One can clearly see from Figure 8 that the absorption coefficient reaches its maximum value at approximately 40 μm. Specifically, the absorption coefficient at 62.5 μm is as large as 0.0724 $\mu m^{-1} = (13.81\ \mu m)^{-1}$. This implies that at the poling period of 7.10 μm only less than four $LiNbO_3$ domains with the corresponding length of 14.2 μm can effectively contribute to the output power generated by the backward parametric process. When the output wavelength is just reduced from 62.5 μm to 58.8 μm, only a single pair of the domains effectively contributes to the output power. Third, the index of refraction and extinction coefficient of the $LiNbO_3$ crystal become very large when the output wavelength approaches 40 μm. Indeed, even at 58.8 μm, they are 8.03 and 0.75, respectively. As a result, the transmittance is reduced to 39.1% at such a wavelength. All these three factors have defined the effective cutoff wavelength of 62.5 μm measured by us for the PPLN crystal.

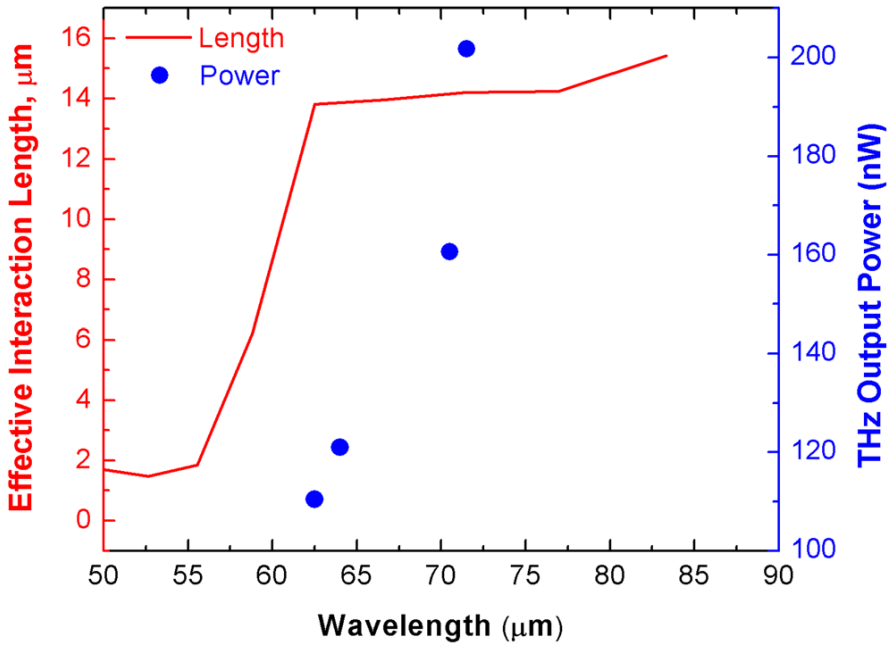

Figure 1.9 THz output power (blue dots) and effective interaction length (red curve) are plotted versus wavelength based on Ref.[1.11].

Despite the fact that the output power is limited by both absorption and reflection, the polariton resonance centered at 40 μm has enhanced the backward parametric process. According to Figure 1.7, we have achieved large enhancements of the output powers in the vicinity of the spectral peaks, generated by the gratings with the periods of 8.60 μm, 8.40 μm, and 7.30 μm relative to those generated by a uniformly poled $LiNbO_3$ chip (labeled as bulk in Figure 1.7). Among these three gratings, an enhancement of as large as 61.1 at the peak wavelength at the period of 8.40 μm is achieved. To the best of our knowledge, this is the largest enhancement reported on a PPLN crystal. Using the data available [1.13], we have plotted the square of the effective NLO coefficient normalized by the square of the electronic NLO coefficient using Eq. (1); see Figure 1.8. One can see from Figure 1.8 that, as the output wavelength approaches 40 μm, the square of effective NLO coefficient reaches a maximum value of roughly 1800 times of its electronic counterpart, i.e., three orders of magnitude. For the shortest center wavelength that we generated, i.e. 62.5 μm, the

corresponding ratio between effective and electronic counterparts of NLO coefficient is about 54. Such dramatic enhancements on NLO coefficients can be exploited for improving the output powers of high-frequency THz waves.

As shown in Figure 1.9, we have measured the THz output powers generated by the six gratings. We have plotted them together with the effective absorption lengths (i.e. the inverse of absorption coefficient, hence the length of the PPLN domains which effectively contributes to the output power) at each output wavelength. At all output wavelengths, huge absorption coefficient resulting to enormously short effective lengths limits the output power of the THz waves. One can see from Figure 1.9 that the highest output power generated by us is 202 nW from the grating with the poling period of 8.60 μm. This output power is a factor of 15.3 larger than that generated by the uniformly-poled $LiNbO_3$ crystal. Besides this grating, all other gratings exhibit significantly-enhanced THz output powers relative to that from the uniformly-poled $LiNbO_3$ crystal. At the poling period of 8.4 μm, 57.4% of the total power (i.e. 100 nW) was generated within the wavelength range of 60-80 μm. Even at the poling period of 7.10 μm, the output power reaches 110 nW. As mentioned by us above, at such a poling period only four domains effectively contribute to the THz output power. This implies that the output power generated by a single domain with its length being 3.55 μm is 6.90 nW. These high output powers generated within extremely short interaction lengths are confirmations of the enhancement factors mentioned above.

VI. THz Generation Investigation of PPLT

Having investigated THz generation in $LiNbO_3$, we move to the study of THz generation in $LiTaO_3$ using the same mechanism of backward optical rectification. The advantage of utilizing $LiTaO_3$ over $LiNbO_3$ lies in the fact that $LiTaO_3$ has a significantly reduced rate

of optically-induced index change damage due to photorefractive effect [1.15]. According to Ref. [1.15], the optically induced index-change damage increases at rates of 2.8×10^{-3} $cm^2/\mu W$ and 4.9×10^{-4} $cm^2/\mu W$ in $LiNbO_3$ and $LiTaO_3$, respectively. The second advantage is that the poling electric field required for $LiTaO_3$ is one order of magnitude lower than that for $LiNbO_3$ [1.14]. In fact, the coercive fields are 1.7 kV/mm and 21 kV/mm for stoichiometric $LiTaO_3$ and congruent $LiNbO_3$, respectively [1.16]. The third advantage for $LiTaO_3$ is the absence of TPA in the vicinity of 800 nm, since its indirect bandgap is 4.1 eV, corresponding to the wavelength of 302 nm [1.16]. However, $LiTaO_3$ suffers from significantly larger absorption in the THz region, compared with $LiNbO_3$ [1.17]. According to Ref. [1.17], the absorption coefficients are determined to be 120 cm^{-1} and 45 cm^{-1} at 1.6 THz for the extraordinary waves in $LiTaO_3$ and $LiNbO_3$, respectively. This is due to the fact one of the polariton resonance frequencies for $LiTaO_3$ is 6 THz, which is significantly higher than 3.9 THz or $LiNbO_3$. Moreover, the second-order nonlinear coefficient for LiTaO3 is a factor of 2.8 lower than that for $LiNbO_3$ [1.16]. At 800 nm, the indices of refraction for the extraordinary waves are about 2.16 and 2.18 for $LiTaO_3$ and $LiNbO_3$, respectively [1.16], which are close to each other. Considering the larger absorption and reduced nonlinear coefficient for $LiTaO_3$, it is natural for us to believe that $LiTaO_3$ is much inferior to $LiNbO_3$ for THz generation based on optical rectification.

In this section, we demonstrate that PPSLT is capable of generating narrowband THz pulses with the output powers of approaching 100 μW based on backward optical rectification using ultrafast laser pulses. Since $LiTaO_3$ has a bandgap of 4.1 eV (i.e., 302 nm), TPA in the vicinity of 800 nm is completely eliminated unlike ZnTe. Moreover, its photorefractive damage effect is much weaker than $LiNbO_3$. Even though $LiTaO_3$ has its

nonlinear coefficient d_{33} of being a factor of 2.8 lower than that for $LiNbO_3$, the output powers generated by these two nonlinear media are within the same order of the magnitude. Following our analysis, we have attributed the enhancements of the THz output power from PPSLT to the enhancements in the second-order nonlinear coefficients. They originate from the polariton resonance due to the presence of transverse-optical (TO) phonons at the frequency of 127 cm^{-1}. Such TO phonons could be induced by nonlinear mixing of two TO phonons at the frequencies of 201 cm^{-1} and 74 cm^{-1}. By significantly reducing the poling periods, we have observed the complete resonant peaks at 127 cm^{-1} (78.7 μm).

The beam diameter of the pump was measured to be 78.8 μm. The highest average power of the pump source used in our experiment is 1.36 W. We measured the spectra of the backward-propagating THz waves generated by the PPSLT gratings in the first wafer, see Figure 1.10. The spectra were directly recorded by a homemade THz grating spectrometer [1.14], which has the frequency error of ±0.5 GHz. The center wavelengths for the backward THz signals were measured to be in the range of 94.0–111.3 μm (3.191 − 2.695 THz) for the eight PPSLT gratings, and the corresponding experimental results are summarized in Table 1.2. For comparison, the spectra of the backward-propagating THz waves generated by PPLN gratings under the same pump conditions are shown in Figure 1.11. The center output wavelengths from the five PPLN gratings were measured to be in the range of 79.3–94.3 μm, see Table 1.2.

Table 1.2. Measurements of Backward THz Waves on First PPSLT Wafer* and PPLN Wafer PPSLT PPLN

	PPSLT								PPLN				
Λ (μm)	10.0	10.4	10.8	11.0	11.2	11.4	11.8	12.0	10.0	10.5	11.0	11.5	12.0
P_{THz} (μW)	3.54	3.46	6.71	3.52	3.99	3.99	3.83	4.39	4.56	6.74	5.69	5.49	4.42
λ_{peak} (μm)	94.0	98.1	102.9	103.4	104.6	105.5	108.8	111.3	79.3	84.6	87.1	90.1	94.3
ν_{peak} (THz)	3.191	3.058	2.915	2.901	2.868	2.844	2.757	2.695	3.783	3.546	3.444	3.330	3.181
$\Delta\nu$ (GHz)	394.4	325.2	327.8	286.8	241.4	238.0	313.9	334.0	853.2	507.9	379.4	383.7	536.2
L_{eff} (μm)	71.7	86.6	85.1	98.5	117.8	120.6	91.8	85.8	39.3	64.9	88.4	88.4	63.1

*Λ, P_{THz}, λ_{peak}, ν_{peak}, Δν, and L_{eff} are poling period, average THz output power, THz output peak wavelength, THz output peak frequency, frequency linewidth of the THz output, and effective interaction length of the nonlinear crystal, respectively.

Based on the published data of phase indices of refraction [1.13, 1.18], the dispersion relations of phase indices of refraction in corresponding THz region of extraordinary beams can be calculated by using the following Sellmeier equations, for $LiTaO_3$ and $LiNbO_3$, respectively:

$$n^2(\lambda) = 44.36 + \frac{3.51 \times 10^4}{\lambda^2 - 3017.75} - 8.00 \times 10^{-5}\lambda^2 \qquad (4)$$

$$n^2(\lambda) = 25.55 + \frac{5.72 \times 10^4}{\lambda^2 - 514.6} - 4.53 \times 10^{-8}\lambda^2 \qquad (5)$$

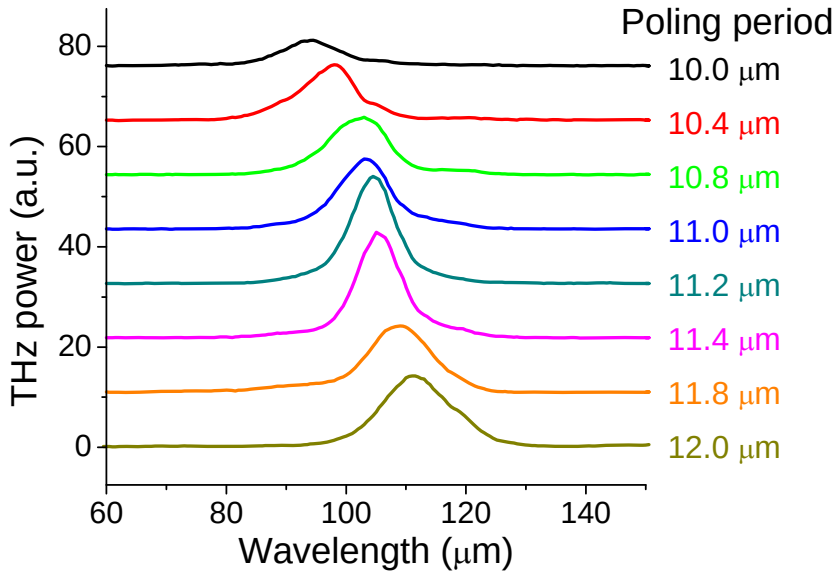

Figure 1.10 Spectra of backward THz radiation measured on 8 PPSLT gratings fabricated on the first PPSTL wafer. The spectrum is equally spaced shifting for clarity. For each spectrum, average over each set of measurements was made.

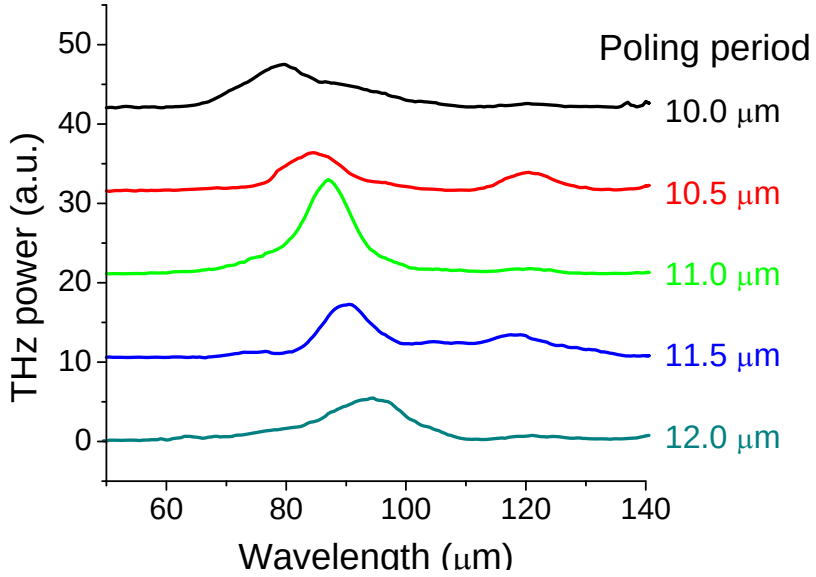

Figure 1.11 Spectra of backward THz radiation measured on 5 PPLN gratings fabricated on one LiNbO3 wafer. The spectrum is equally-spaced shifting for clarity.

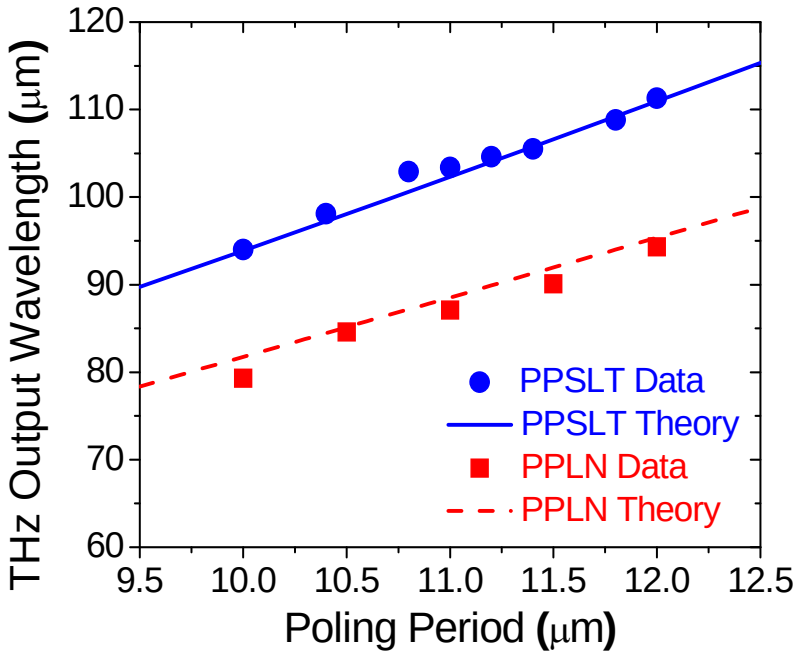

Figure 1.12 Experimental results of peak wavelengths of backward THz radiation from PPSLT gratings of the first wafer (dots) and PPLN gratings (squares), corresponding theoretical dependence (solid curve for PPSLT and dashed curve for PPLN) based on Eqs. (3) and (4), and (3) and (5), respectively.

By substituting indices of refraction given by Eqs. (4) and (5) above into Eq. (3), respectively, the peak wavelengths of the backward THz radiation from PPSLT and PPLN can be calculated.

The corresponding values are consistent with the values determined from the experiment, see Fig. 1.12. One can see from Fig. 1.12 that our experimental data of the peak wavelength of the backward THz radiation are in good agreements with the theoretical values for both PPSLT and PPLN. On the other hand, the linewidth of each backward THz quasi-phase matched peak can be determined by the following expression:

$$\Delta\nu_{\mathrm{THz}} \approx \frac{2\mathrm{sinc}^{-1}(\frac{1}{\sqrt{2}})c}{\pi(n_{\mathrm{pg}} + n_{\mathrm{tg}})L_{\mathrm{eff}}} \qquad (6)$$

where n_{tg} is the THz group velocity, c is the speed of light, and L_{eff} is the effective interaction length of the nonlinear crystal. If we neglect the differences between the phase and group indices of refraction for the THz radiation, the effective interaction length of each PPSLT and PPLN grating can be readily deduced from the measured spectra of THz radiation, see Figs. 1.10 and 1.11,

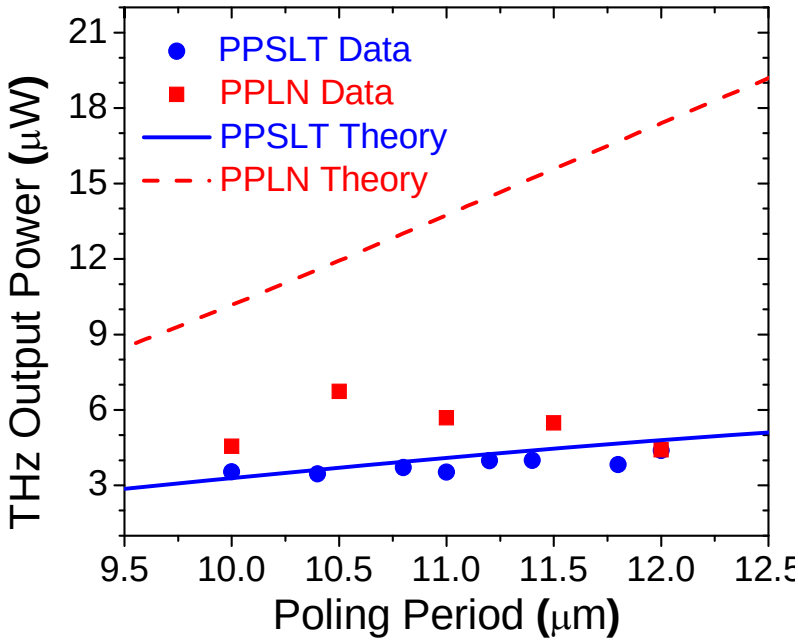

Figure 1.13 Experimental results of backward THz output powers from PPSLT gratings (dots) and PPLN gratings (squares), corresponding theoretical dependence (solid curve for PPSLT and dashed curve for PPLN, respectively) based on Eq. (8).

and Table 1.2. Based on above estimation, the effective interaction lengths of PPSLT and PPLN gratings are between 39.3 and 120.6 μm. Such short effective interaction lengths are resulted from the large absorption coefficients of $LiTaO_3$ and $LiNbO_3$ at corresponding wavelength. Moreover, with the same or equivalent poling period, the effective interaction length of PPSLT grating is obviously longer than that of PPLN grating. Under the pump intensity of 13.9 kW/cm^2, the highest output powers of THz radiation were measured to be

in the range from 3.46 to 4.39 μW for the eight PPSLT gratings, see Table 1.2. In comparison, the highest output powers are in the range from 4.42 to 6.74 μW for the five PPLN gratings, respectively, see Table 1.2. Regardless of the effect of the interaction length on the nonlinear optical process and the absorption of the THz waves in nonlinear crystals, the amplitude of the backward THz electric field, E_{THz}, can be described by the simplified model [1.11, 1.12]:

$$E_{\mathrm{THz}} = \frac{4\pi^2 c^2 d_{33} \tau^2 E_0^2}{n(\lambda_{\mathrm{THz}})[n_{\mathrm{pg}} + n(\lambda_{\mathrm{THz}})]\lambda_{\mathrm{THz}}^2 \sinh\left(\pi^2 c\tau/\lambda_{\mathrm{THz}}\right)} \qquad (7)$$

where E_0 and τ are the amplitude and effective pulse width of the pump pulses, respectively. The corresponding intensity of the backward THz wave can be calculated by using the following expression:

$$I = \frac{n(\lambda_{\mathrm{THz}}) E_{\mathrm{THz}}^2}{2\eta_0} \qquad (8)$$

where η_0 is vacuum impedance. According to Eqs. (5) and (6), we can estimate the backward THz output power as a function of the poling period of the nonlinear crystals, as shown in Fig. 1.13 One can see that the backward THz output power measured in our experiment for the PPSLT gratings are consistent with the theoretical curve whereas the THz output power for the PPLN gratings are much lower than the theoretical results. Although the second-order nonlinear susceptibility (only the element, d_{33}, used for the THz generation) of $LiNbO_3$ is about 2.8 times higher than that of $LiTaO_3$ [1.14], the THz output power from PPLN gratings are comparable to that of PPSLT gratings, especially for the gratings with longer poling periods. We believe that TPA of pump photons in $LiNbO_3$ may play important role in the reduction of backward THz output power from PPLN gratings.

Among all eight PPSLT gratings, the highest backward THz output power was measured to be 4.39 μW from grating with the poling period of 12.0 μm, see Table 1.2, which corresponds to the pulse energy of 17.6 pJ. According to Eq. (1.4), the phase index of refraction for THz frequency at 2.695 THz is about 7.07. Therefore, the Fresnel loss of THz wave at the PPSLT-air interface is 56.6%. Moreover, the collection efficiency which is determined by the aperture of parabolic mirror in our experimental setup is 10.6%. After taking into consideration all the factors above, we can estimate the highest average power of the backward THz radiation which is generated inside the PPSLT grating with a poling period of 12.0 μm to be 95.7 μW, which corresponds to the pulse energy of 0.38 nJ. Such an output power corresponds to the photon conversion efficiency of ~1%. Based on our previous measurement [1.14], the photon conversion efficiency in backward optical rectification process can be readily to increase to ~30%.

Although the lengths of the PPSLT and PPLN crystals are not the same, our comparison made on two crystals still makes sense. This is due to the fact that for the THz waves generated by these crystals only the THz powers generated within the lengths of 39.3–120.6 μm measured from the entrance facets for the laser radiation can be coupled out, see Table 1.2. Basically, due to high absorption coefficients, the crystal lengths have become irrelevant.

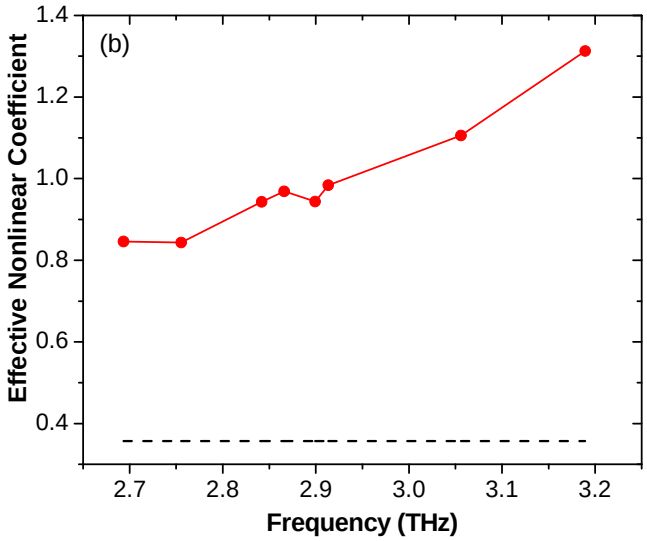

Figure 1.14 Effective nonlinear coefficient for PPSLT, normalized by that for PPLN and deduced from experimental results (dots) and from optical domain (dashed line) versus frequency. The plot illustrates the increase of the effective nonlinear coefficient for PPSLT with increasing frequency.

As discussed above, compared with the output powers from the PPLN wafers, the output powers generated by the PPSLT wafers are lower by 20%. However, this contradicts what we have predicted based on the major differences between the two nonlinear media in terms of absorption coefficients in the THz region and nonlinear coefficients used for THz generation. According to Ref. [1.15], the effective nonlinear coefficients of the PPLN gratings can be approximated by a constant within 94.0–111.3 μm. It is worth noting that in Table 1.2 the center output wavelength for the poling period of 10.0 μm for the first PPSLT wafer is measured to be 94.0 μm, which is close to 94.3 μm for the PPLN grating at the poling period of 12.0 μm. Since the THz output power is proportional to the square of the THz electric field, we are able to determine the effective nonlinear coefficients of the PPSLT grating normalized by that of the PPLN grating at 94.3 μm using Eq. (1.7), see Fig. 1.14. As mentioned above, in the optical frequency range, the electronic counterpart

of nonlinear coefficient dominates while the ionic one is negligible. It turns out that the effective nonlinear coefficient for PPSLT is a factor of 2.8 lower than that for PPLN, see the dashed line in Fig. 1.14. On the contrary, in the THz range the ratios of the nonlinear coefficients between PPSLT and PPLN are calculated to be factors of 0.85–1.31. Therefore, the nonlinear coefficients for PPSLT are enhanced by factors in the range of 2.4–3.7, compared with that for PPLN. This implies that the THz output powers are enhanced factors of 5.1–13.5, since the THz output power is proportional to the square of the effective nonlinear coefficient, see Eq. (7) above.

According to Fig. 14, the nonlinear coefficient approaches a resonance peak as the THz frequency is increased. For simplicity, let us consider only one polariton resonance. The effective second-order nonlinear coefficient can be determined by the following expression [1.19]:

$$d_{\text{eff}} = d_{\text{e}}\left[1 + S_{\text{rel}}\frac{\nu_0^2}{\nu_{\text{TO}}^2 - \nu^2 - i\nu\Gamma}\right] \qquad (9)$$

where d_{e} is the electronic coefficient, S_{rel} is the relative oscillator strength describing the contribution of the ionic movement to the effective second-order nonlinear coefficient, ν_{TO} and Γ are TO phonon frequency and linewidth of the polariton resonance. According to Ref. [1.20], there are four TO phonons for PPSLT at the frequencies of 74 cm^{-1}, 140 cm^{-1}, 201 cm^{-1}, and 206 cm^{-1}, respectively in the low-frequency end. However, none of these four frequencies can be used to achieve an acceptable fit to the data shown in Fig. 1.15.

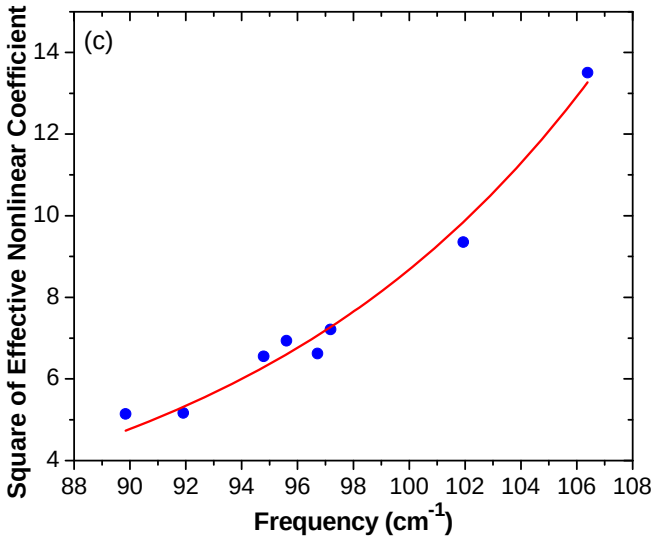

Figure 1.15 Square of nonlinear coefficient for PPSLT, enhanced relative to that of PPLN vs. frequency. The graph illustrates that the squares of the effective nonlinear coefficients for PPSLT can be up to one order of magnitude larger than those for PPLN, resulting in the comparable output powers for PPSLT and PPLN.

In Ref. [1.7] it was stated that $LiTaO_3$ exhibits strong anharmonicity, i.e., its potential energy has a severe non-parabolic shape as a function of Li+ displacement. In such a case, two TO frequencies can be mixed through the anharmonicity to generate a beat phonon frequency. As described in Ref. [1.8], a new resonance frequency at 31.7 cm^{-1} (i.e., 0.95 THz) is observed, which was attributed to the tunneling resonance between two adjacent potential wells. It turns out that in our case, only a new frequency of 127 cm^{-1} can be used to obtain a reasonably good fit to the data points, see Fig. 1.14. As a result of the nonlinear least-square fit, we have obtained $S_{rel} \approx 0.051$ and $\Gamma \approx 34.69$ cm^{-1}, respectively. We believe that this new polariton resonance at 127 cm^{-1} is the origin of the enhancement of the backward THz powers generated by PPSLT. According to Eq. (7), the output power can further increase by three times at the peak of the resonance. This can be achieved by

designing the poling period to be 8.2 μm. As mentioned above, due to the strong anharmonicity, this new frequency can be induced by nonlinear mixing of the phonons at the frequencies of 201 cm^{-1} and 74 cm^{-1}.

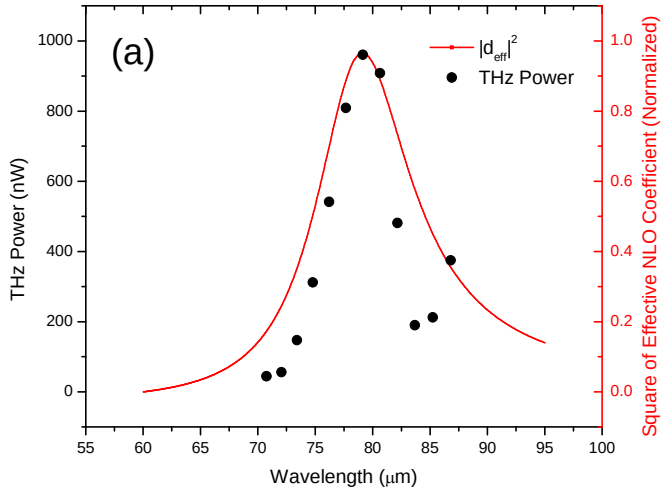

Figure 1.16 Dots: THz powers generated by all gratings of the second PPSLT wafer, red curve: square of effective nonlinear coefficient is plotted illustrating the strong resonance at 79 μm. They illustrate that we have reached the complete resonance for PPSLT.

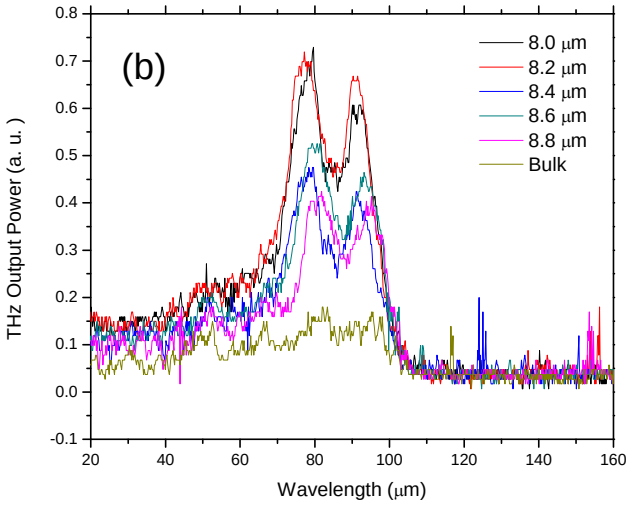

Figure 1.17 Spectra from 5 of gratings; spectrum form bulk (uniformly poled) crystal is plotted as a reference. Each spectrum was obtained after a single measurement. One can see the "double-peak" feature in this spectrum.

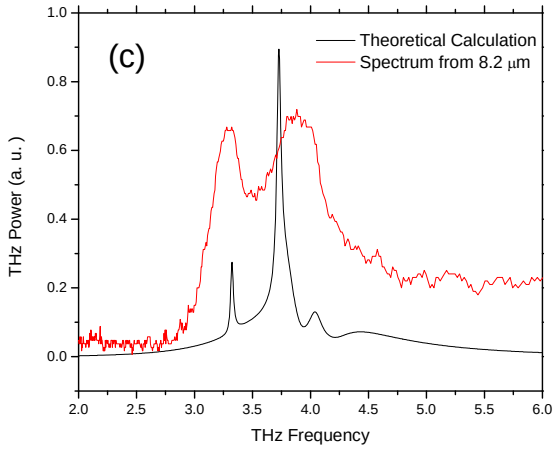

Figure 1.18 Theoretical calculation (black) is used to support the "double-peak" feature of the experimental spectrum (red). One can see that we have qualitatively explained the origin of the "double-peak" feature.

To support the proposed mechanism of nonlinear mixing of two transverse-optical phonons through strong anharmonicity of $LiTaO_3$, we have investigated the THz generation from the second wafer having significantly shorter periods than those in the first wafer. We are hoping that we are able to observe the entire resonance at the frequency of 127 cm−1 (78.7 μm).

We measured the THz output power generated by 12 gratings, as shown in Fig. 1.16. The wavelength was determined based on the quasi-phase-matching condition for the backward THz generation. The highest THz power generated was about 960 nW at 79.14 μm, which was generated by the grating at the poling period of 8.2 μm. Compared with our previous work on $LiNbO_3$ [1.21], such power was nearly 4 times larger than the 201.8 nW at 75.5 μm, which was in a very close wavelength regime. Compared with the output powers at the shorter wavelengths, the enhancement factors reach 22.8. This result confirmed our prediction made on the first PPSLT wafer that the effective second-order nonlinear

coefficient is enhanced by the polariton resonance caused by the phonons having the frequency of 3.81 THz (78.7 μm) due to nonlinear mixing of two TO phonon frequencies of $LiTaO_3$. As mentioned above, the two TO phonon frequencies at 6.0 THz and 1.19 THz undergo nonlinear mixing through anharmonicity. As a result, a beat phonon frequency is generated at 3.81 THz. Using Eq. (9), the square of the nonlinear coefficient is plotted in Fig. 1.16 (red), illustrating that the highest THz output power coincides with the peak of the nonlinear coefficient. We measured the spectra of the backward-propagating THz pulses generated by the 12 PPSLT gratings. Among them, five spectra from the gratings with the poling periods of 8.0, 8.2, 8.4, 8.6, and 8.8 μm, respectively, exhibited distinguished peaks, as shown in Fig. 1.17. The spectrum from bulk (uniformly poled) $LiTaO_3$ crystal was plotted in Fig. 1.17 as the reference. One can see from Fig. 1.17 that periodic poling is essential for the observation of the two distinct peaks in the spectra. According to quasi-phase-matching condition for the backward THz generation, these gratings are expected to generate THz pulses at the center wavelengths of 77.67, 79.14, 80.64, 82.16, and 83.69 μm, respectively. However, the "double-peak" feature appears in the spectrum for each THz pulse, the center wavelengths of these two peaks being measured as 77.3 and 90.5 μm. To understand the origin of such a unique feature, we start with the output power of the THz radiation [1.22]

$$P_{\mathrm{THz}} = \frac{1}{2}\sqrt{\frac{\epsilon_0}{\mu_0}}\sqrt{\epsilon_{\mathrm{THz}}}|E_{\mathrm{THz}}|^2 AT \qquad (10)$$

where A is the area, T is the transmittance for the THz radiation generated by $LiTaO_3$ crystal due to the reflection at the crystal/air interference, and E_{THz} is the electric field amplitude of THz radiation, which is given by [1.22]

$$E_{\mathrm{THz}} = -i\omega_{\mathrm{THz}}\sqrt{\frac{\mu_0}{\epsilon_0}}\frac{d_{\mathrm{eff}}}{\sqrt{\epsilon_{THz}}}|E_{\mathrm{p}}|^2\left[\frac{\exp\left(-i\Delta k/L\right)-\exp\left(-\alpha L/2\right)}{\alpha/2-i\Delta k}\right] \quad (11)$$

where E_{p} is the electric field amplitude of the pump beam, α is the absorption coefficient, L is the effective interaction length, and Δk is the wave vector mismatch. The last term in square brackets represents the contribution of absorption and phase mismatching. To calculate $\varepsilon_{\mathrm{THz}}$, α, and T, the frequency dependent complex dielectric function can be represented by a

Lorentz model [1.23]:

$$\epsilon(\nu) = \epsilon_\infty + \frac{S_0\nu_0^2}{\nu_0^2-\nu^2-i\nu\Gamma} = \hat{n}^2 = (n+i\kappa)^2 \quad (12)$$

where ϵ_∞ designates the bound electron contribution to the dielectric function. By evaluating the real and imaginary parts we have obtained the index of refraction, n, and the power absorption coefficient $\alpha = 4\pi\kappa\nu$. Based on such a model, we have produced a reasonable fit to the observed spectrum, as shown in Fig. 1.18 in red. The black curve is the experimental spectrum from grating of 8.2 μm. As a result of the fitting, we have obtained $S_0 \approx 1.2$ and $\Gamma \approx 0.5$ THz. Thus, we can attribute the origin of this "double-peak" feature to the combination among effective nonlinear coefficient, absorption, and transmittance in the polariton resonance regime. The broadening of the peaks in the experimental spectrum originates from the fabrication error of the grating.

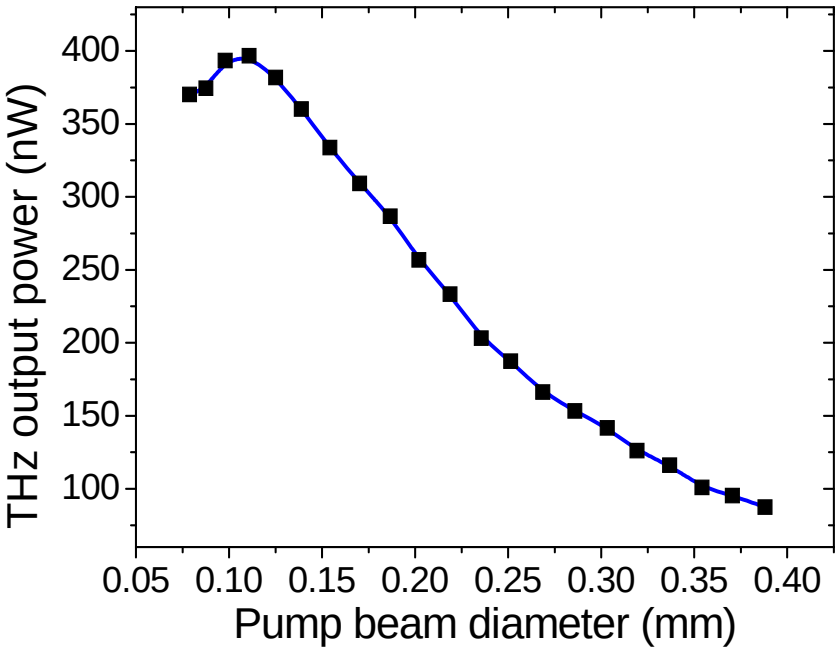

Figure 1.19 Backward THz output power from PPSLT grating with poling period 11.2 μm as a function of pump beam diameter at entrance crystal. Squares are experimental data with a constant pumping power of 400 mW, and the solid curve's purpose is to guide the eye.

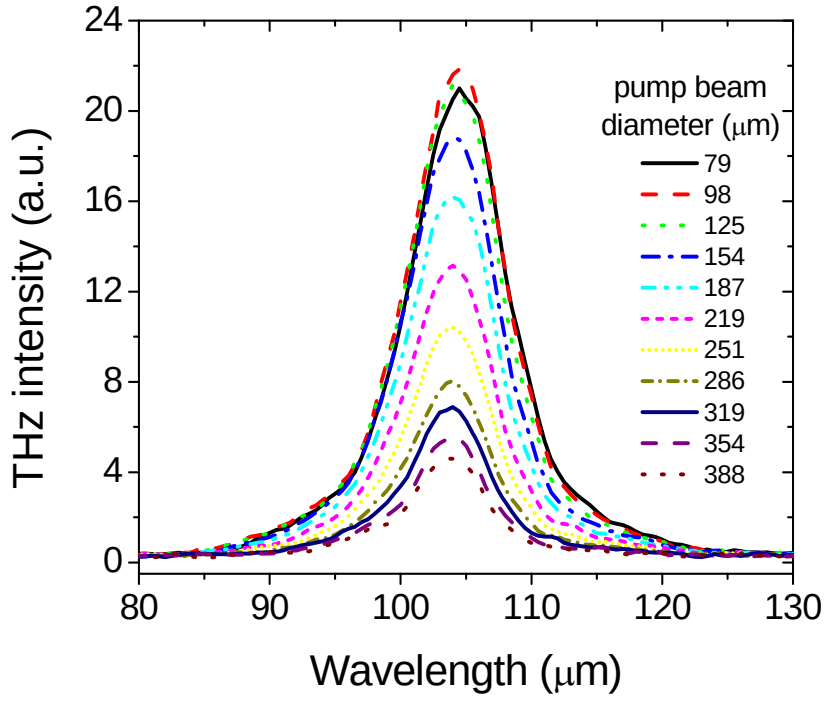

Figure 1.20 Spectra of backward THz radiation from PPSLT grating (Λ=11.2 μm) at different pump beam size. Pumping power is kept at 400 mW and pump beam diameters vary from 78.8 to 388 μm.

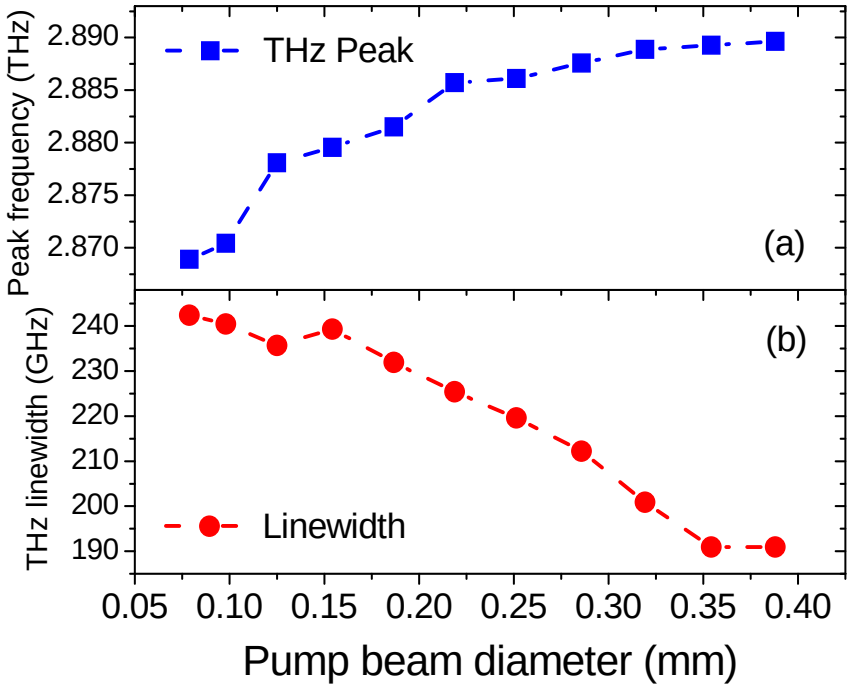

Figure 1.21 (a) Peak frequency (squares) and (b) linewidth (dots) of backward THz radiation from PPSLT grating ($\Lambda \approx 11.2$ μm) as a function of pump beam diameter. The dashed lines' purpose is to guide the eye.

To further investigate the optimal pump condition for the backward THz generation from PPSLT, we have investigated the dependence of the THz spectra and output powers on the beam size of the pump in our experiment. To avoid damage of the PPSLT crystal by the pump laser at the high intensity achieved at the small beam size and reduce thermal effects, we have kept the pumping power at 400 mW or lower throughout our measurements. Following our measurements, we have plotted the output power vs. the beam diameter for the grating period of 11.2 μm in Fig. 1.19. One can see from Fig. 1.19 that with decreasing the beam diameter from 388.0 to 110.8 μm, the THz output power is monotonously increased from 87 to 397 nW, i.e., by a factor of 4.6. However, as the diameter is further decreased from 110.8 μm, the output power is decreased from 397 to 370 nW, i.e., by 6.8%. Therefore, for the grating period of 11.2 μm, an optimal diameter of the pump beam is

110.8 μm. In comparison, under the same experimental conditions the PPLN grating having the poling period of 11.0 μm exhibits a similar behavior. Since the peak wavelengths generated by these two gratings are 104.6 and 87.1 μm, we have attributed the existence of the optimal diameters to the competition between the divergence of the THz output beam and quadratic dependence of the THz output power on the pump intensity. Indeed, as the diameter of the pump beam is decreased, the THz output power becomes more divergent. Therefore, the amount of the THz output power being coupled out of the crystal is decreased. This effect is completely opposite to the quadratic increase of the THz output power due to the increase of the intensity of the pump beam.

We have measured and plotted the spectra of the THz radiation at different diameters of the pump beam in Fig. 1.20. When the diameter is increased from 78.8 to 388.0 μm, the peak wavelength is slightly decreased from 104.6 to 103.8 μm, i.e., the peak is just blue-shifted from 2.869 to 2.890 THz, see Fig. 1.21(a). This corresponds to the amount of the blueshift to be 21 GHz, which is less than 1% of the center frequency. This blueshift originates from the weak thermal effect as the diameter is reduced. It is consistent with the blueshift observed by decreasing the pump power while fixing the beam diameter. On the other hand, the linewidth of the peak, determined at FWHM, is decreased from 242 to 191 GHz, i.e., by the amount of 52 GHz or 21%, see Fig. 1.21(b), as the diameter of the pump beam is increased from 78.8 to 388.0 μm. The smaller the pump beam diameter, the larger the divergent angle for the THz output beam, and therefore, the shorter the effective interaction length for the optical rectification. According to Eq. (6), the linewidth is increased, and the diameter is broadened.

VII. Conclusion and Outlook

In conclusion, we have demonstrated efficient generation of short-wavelength THz pulses from PPLN wafer containing multiple poling periods by using a femtosecond laser amplifier. The record-short center wavelength generated by us is 62.5 μm at the poling period of 7.10 μm. Higher output powers are feasible when approaching the polariton resonance at 40 μm and employing a novel configuration [1.24, 1.25].

We have also achieved highly efficient generation of backward THz pulses in the frequency range of 2.695-3.191 THz from PPSLT using the same experimental setup at the PPLN work. Although the effective second-order nonlinear coefficient of $LiTaO_3$ is a factor of 2.8 lower than that of $LiNbO_3$ in the optical frequency range, the THz output powers from the PPSLT gratings are within the same order of magnitude as those from the PPLN gratings. The highest THz output power for PPSLT gratings approached 100 μW. The enhancements of the THz output powers from the PPSLT gratings can be attributed to the enhancements in the second-order nonlinear coefficients. Based on our analysis, we conclude that the nonlinear coefficients are enhanced by the polariton resonance at the frequency of around 127 cm^{-1}. Such a phonon frequency can be generated by the nonlinear mixing of two TO phonons at the frequencies of 201 cm^{-1} and 74 cm^{-1} due to strong anharmonicity of $LiTaO_3$. We have observed the complete resonant peak at the second wafer having significantly shorter poling periods.

Moreover, we demonstrated the competition between the divergence of the THz output beam and quadratic dependence of the THz output power on the pump intensity, resulting in the optimal diameters of the pump beam. When the diameter of the pump beam is

increased from 78.8 to 388.0 μm, the linewidth of the THz peak is reduced by 52 GHz whereas the peak frequency is slightly blue-shifted by 21 GHz.

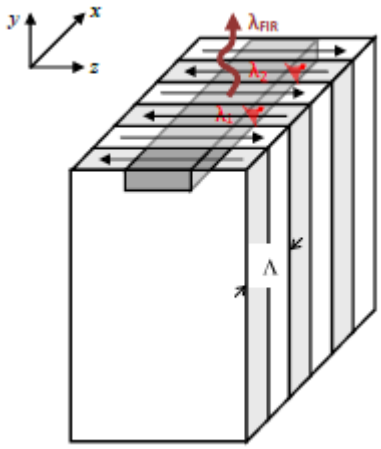

Figure 1.22 Surface emitting configuration for THz generation. Figure cited from Ref. [1.24]

There are still flaws in our current scheme that would limit the THz emission efficiency. Since the polariton resonance has effects on any order of indices, it would also induce severe absorption, short effective interaction length, and poor transmittance of THz waves near resonance frequency. To detour from this roadblock, a surface emitting configuration can be applied a novel generation method [1.24]. As shown in Figure 1.22, the THz waves would radiate perpendicular to the direction of pump beam propagation, thus avoiding being absorbed since the sickness of the media can be comparable to THz wavelengths. Also, to improve the interaction length inside the media, waveguides of pump beams can be designed for a high optical density in the active region, resulting in better THz conversion efficiency.

Chapter 2 Device Thermal Management by Raman Scattering

I. Introduction

a. A Survey of High Electron Mobility Transistor (HEMT) Materials

As the market for cellular, personal communications services, and broadband access are expanding and the realization of 4G LTE technologies, radio frequency and microwave power amplifiers are attracting numerous attentions in both academics and industry. Several types of power amplifier technologies are competing for market share, such like Si lateral-diffused metal-oxide-semiconductors and bipolar transistors, GaAs metal-semiconductor field-effect transistors (MESFETs), GaAs (or GaAs/InGaP) heterostructure bipolar transistors, SiC MESFETs, and GaN HEMTs.

Table 2.2 Properties of Competing Materials in Power Electronics (refromed from Ref. [2.1]).

Material	**μ**	**ε**	**E_g (eV)**	**BFOM Ratio**	**JEM Ratio**	**T_{max} (°C)**
Si	1300	11.4	1.1	1.0	1.0	300
GaAs	5000	13.1	1.4	9.6	3.5	300
SiC	260	9.7	2.9	3.1	60	600
GaN	1500	9.5	3.4	24.6	80	600

The properties of GaN materials comparing to the competing ones is presented in Table 2.1 [2-1]. The resulting competitive advantages of GaN devices and amplifiers for a commercial product are described in Table 2.2. From these two tables, we can see that in every single category, GaN devices excel over conventional technology. Most significantly, GaN materials properties of direct wide bandgap, high breakdown field, high operating voltage, and compatibility with SiC substrate would enable performance advantages in compactness, easy matching, elimination of step-down, power saving and cooling

reduction, high power operation, suitability for lighting, and lower cost. All these promising features open up several industrial, automotive, aircraft, and defense applications, as shown in Figure 2.1.

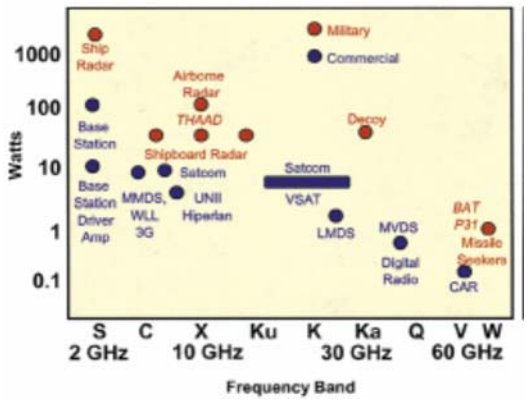

Figure 2.1 Applications of GaN devices (from Ref. [2.1])

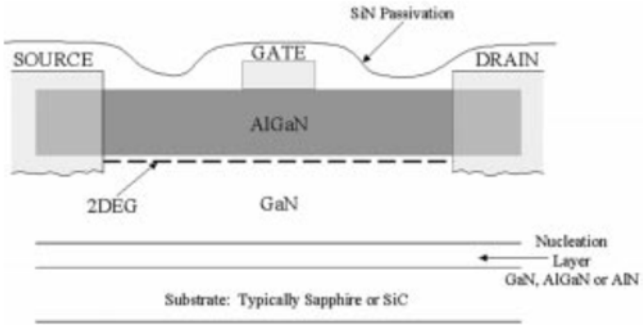

Figure 2.2 Basic GaN HEMT structure (from Ref. [2.1])

The structure of a basic GaN HEMT is shown in Figure 2.2. The epitaxial layers can be grown by molecular beam epitaxy (MBE) or metal-organic chemical vapor deposition (MOCVD). It has been shown that easy growth and fabrication can be realized for the production of GaN HEMT devices.

In conclusion, while GaN device and circuit technology is likely poised to break out in the commercial arena, certain risks and barriers to entry in the market cannot be overlooked.

Besides the relative immaturity of GaN with respect to Silicon and GaAs technologies, in academics, the "hot-phonon" issue is the main factor for limiting its performance, which will be discussed in the following subsection.

Table 2.3 Competing advantages of GaN devices (refromed from Ref. [2.1])

Need	**Enabling Feature**	**Performance Advantage**
High Power/Unit Width	Wide Bandgap, High Field	Compact, Ease of Matching
High Voltage Operation	High Breakdown Field	Eliminate/Reduce Step Down
High Linearity	HEMT Topology	Optimum Band Allocation
High Frequency	High Electron Velocity	Bandwidth, μ-Wave/mm-Wave
High Efficiency	High Operating Voltage	Power Saving, Reduced Cooling
Low Noise	High Gain, High Velocity	High dynamic range receivers
High Temperature Operation	Wide Bandgap	Rugged, Reliable, Reduced Coating
Thermal Management	SiC Substrate	High Power Devices with Reduced Cooling Needs
Technology Leverage	Direct Bandgap Enabler for Lighting	Driving Force for Technology: Low cost

b. "All about Hot Phonons"

Due to very large direct bandgap (3.4 eV), GaN has longitudinal optical (LO) phonons with relatively large energies of roughly 91 meV [2.2]. Such high LO phonon energy results in a wide bandgap between the optical branch and the acoustic branch of GaN phonon bandstructure. This kind of phononic bandstructure leads to the lack of decay

channels for LO phonons in GaN devices generated through Fröhlich Interaction. Thus, large numbers of non-equilibrium LO phonons, i.e. the so called "Hot Phonons", would accumulate in regions of carrier transport in GaN HEMTs, strongly deteriorating the performance of such devices. Specifically, the emission time of LO phonon generated through Fröhlich Interaction is in the range from 10 to 50 fs [2.3, 2.4], while its decay time can be as large as 1 to 5 picoseconds (ps) [2.5~2.7], which is 2 orders of magnitudes larger. The tremendous difference between LO phonon emission and decay time creates the "phonon decay bottleneck", resulting in an electron drift velocity saturation at 1.5×10^7 cm/s [2.8]. This bottleneck will eventually limits GaN devices' high operating power and temperature. It is obvious that the study of hot phonons behaviors and methods of reducing hot phonons effect is urgently required for the development of GaN HEMTs. In the following subsection, I will discuss two methods of measuring hot phonon temperatures through the utilization of Raman Scattering.

II. Theory of Measuring Phonon Temperature

Since Raman Scattering results from the interaction of a laser beam and optical phonons, the properties of Stokes and Antistokes Raman spectra would certainly carry information of hot phonons generated by Frohlich interactions. Typically, there are two ways of temperature measurement derived from Raman Scattering properties

a. Raman Ratio Method

The first way of measuring hot phonon temperature is by the ratio of intensities between Antistokes and Stokes Raman Scattering. The relationship between Stokes (Antistokes)

Raman photon number N_s (N_{as}) and the phonon number N_p can be described as the following

$$N_s = \sigma_s N_i (N_p + 1), \quad N_{as} = \sigma_{as} N_i N_p \tag{1}$$

Here, N_i is the photon number of incident laser, σ_s (σ_{as}) is the Raman Scattering cross-section of the Stokes (Antistokes) process. The phonon number obeys the Bose-Einstein distribution, which can be expressed as the following

$$N_p = \frac{1}{\exp\left(\frac{\hbar\omega_{\mathrm{LO}}}{kT_{\mathrm{LO}}}\right) - 1}. \tag{2}$$

Since the optical intensity is proportional to its corresponding photon number, the ratio of Antistokes and Stokes photon number is equal to the ratio of intensities between the two. This is a quantity that can be measured in experiment directly:

$$\frac{I_{as}}{I_s} = \frac{N_{as}}{N_s} = \frac{\sigma_{as} N_p}{\sigma_s (N_p + 1)} \tag{3}$$

It is obvious that if the two cross-section equals, the fraction can be further simplifies as the following

$$\frac{I_{as}}{I_s} = \frac{N_p}{N_p + 1} = \exp\left(-\frac{\hbar\omega_{\mathrm{LO}}}{kT_{\mathrm{LO}}}\right). \tag{4}$$

From Eq. (4), we can see that once we have the ratio of Antistokes and Stokes Raman Intensities, the phonon temperature can be extracted from the exponential. It is shown that only if the initial state of Stokes process is the final state of Antistokes process, while the final state of Stokes process is the initial state of Antistokes process, [2.9] the two cross-sections are equal, as shown in the following expressions and Figure 2.3:

$$\sigma_s \propto \left(\frac{1}{\hbar\omega_{\mathrm{LO}}}\right)\left|\frac{1}{E_g - \hbar\omega_i - \hbar i/\tau} - \frac{1}{E_g - \hbar\omega_s - \hbar i/\tau}\right|^2 \tag{5}$$

$$\sigma_{as} \propto \left(\frac{1}{\hbar\omega_{\mathrm{LO}}}\right)\left|\frac{1}{E_g - \hbar\omega_i - \hbar i/\tau} - \frac{1}{E_g - \hbar\omega_{as} - \hbar i/\tau}\right|^2 \quad (6)$$

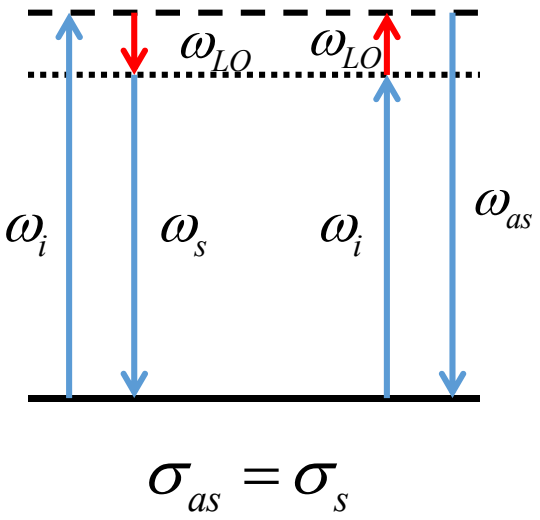

Figure 2.3 Schematic relation of Stokes and Antistokes Raman processes when Raman cross-sections are equal.

This means that to realize the experimental conditions for measuring the phonon temperature, we need an accurate tunable laser to be the incident beam source. Also, since the Raman signal intensity is much weaker than the one of its incident laser (especially the Antistokes signal), it is very difficult to identify the signal from a spectrum since the two lines would be very close in wavelength. To increase the Raman signal strength, a laser

wavelength close to the bandgap of GaN (3.4 eV, 365 nm) would be favored. Since the lack of notch filter in this spectrum region around 365 nm, a spectrometer of superior resolution is needed. Such a spectrometer would usually contain at least two gratings inside in order to distinguish the Raman signal from the laser one, and is usually very expensive.

The advantage of this method of measuring phonon temperature is the simple relationship between experimental measuring quantity (Raman signal strength, can be extracted from integrated peak intensity from spectra) and temperature. Such simple relation is also material irrelevant.

b. Raman Shift Method

Having identifies the merits and flaws of Raman ratio method, we now turn to the theory of another method of measuring phonon temperature which requires a more accessible experimental condition. It is known that due to multiple mechanisms, the energies of E_2 and A_1 (LO) phonons in GaN would experience red shift while temperature rises. If a mathematical dependence between temperature and phonon energy (Raman frequency, as measurable quantity) can be established, the temperature can be deduced from that directly.

According to Ref. [2.10], there are three mechanisms that would cause the red shift of Raman frequency with increasing temperature in GaN. The total temperature dependence of the phonon frequency can be written as the following

$$\omega(T) = \omega_0 + \Delta\omega_e(T) + \Delta\omega_d(T) + \Delta\omega_s(T) \quad (7),$$

Where $\Delta\omega_e(T)$ denotes the frequency shift due to the thermal expansion of lattice. In an isotropic approximation, the term $\Delta\omega_e(T)$ can be written by

$$\Delta\omega_e(T) = -\omega_0\gamma \int_0^T [\alpha_c(\tilde{T}) + 2\alpha_a(\tilde{T})]d\tilde{T} \quad (8),$$

Where α_c and α_a are the temperature dependent coefficients of linear thermal expansion parallel and perpendicular to the c axis, respectively, and γ is the Grüneisen parameter. $\Delta\omega_d(T)$ represents the frequency shift caused by the decay of optical phonon into phonons with lower energy. Taking into account cubic and quartic terms in the anharmonic Hamiltonian and considering only symmetric decays of the zone-center phonons into two phonons (third-order process) and three phonons (fourth-order process) with frequencies $\omega_0/2$ and $\omega_0/3$, respectively, the term $\Delta\omega_d(T)$ is given by

$$\Delta\omega_d(T) = A[1 + 2n(T, \omega_0/2)] + B[1 + 3n(T, \omega_0/3) + 3n^2(T, \omega_0/3)] \quad (9),$$

Where $n(T, \omega) = [\exp(\hbar\omega/k_B T) - 1]^{-1}$ is the Bose-Einstein distribution function and *A* and *B* are coefficients. Due to the considerable lattice and thermal mismatch between the substrate and the GaN layers, the third term in Eq. (7), $\Delta\omega_s(T)$, is the strain-induced contribution to the phonon frequency shift. To estimate $\Delta\omega_s(T)$, we assume that during the post-growth cooling, the different thermal expansion coefficients of layer and substrate result in a temperature-dependent in-plane strain

$$\epsilon(T) = \frac{L_S(T) - L - L(T)}{L - L(T)} = (1 + \epsilon_g)\frac{1 + \int_{T_g}^{T} \alpha_{a,S}(\tilde{T})d\tilde{T}}{1 + \int_{T_g}^{T} \alpha_{a,L}(\tilde{T})d\tilde{T}} - 1 \quad (10),$$

Where $\alpha_{a,S}$ and $\alpha_{a,L}$ are the temperature-dependent in-plain linear expansion coefficients of the substrate (*S*) and the layer (*L*), respectively. $L_{S,L}(T) = L_{S,L}(T_g)[1 + \int_{T_g}^{T} \alpha_{a,S,L}(\tilde{T})d\tilde{T}]$ denotes the temperature-dependent lengths of the substrate and the layer without having any contact to each other, and ϵ_g is the residual strain in the layer at growth temperature T_g. With the phonon deformation potentials *a* and

b, and the elastic constants C_{13} and C_{33} of the layer, the frequency shift due to the layer mismatch $\Delta\omega_s(T)$ can be written by

$$\Delta\omega_s(T) = 2\left(a - b\frac{C_{13}}{C_{33}}\right)\epsilon(T) \qquad (11).$$

With $\Delta\omega_e(T)$, $\Delta\omega_d(T)$, and $\Delta\omega_s(T)$ established in Eqs. (8, 9, 11), we can utilize Eq. (7) to fit the measured phonon frequencies and hence deduce the phonon temperature. Obviously, this method only requires the stronger Stokes Raman signal, and there is no need to tune the pump laser back and forth to meet the requirement of the same Raman cross-sections, as in the Raman ratio method. Also, a double- or triple-grating spectrometer is no longer necessary. A simple long-pass filter can be used to block the pump laser signal and reveal the Stokes Raman signal. The complexity of this method lies in the fact of its material dependence. Various parameters including thermal expansion coefficients, Grüneisen parameter, residual strain, and elastic constant would be required to ensure the accuracy of the fitting and extracting of temperature. Strictly speaking, a pre-measured calibration curve would be necessary for each single sample with its unique substrate information and growth condition.

III. Sample Information and Experimental Setup

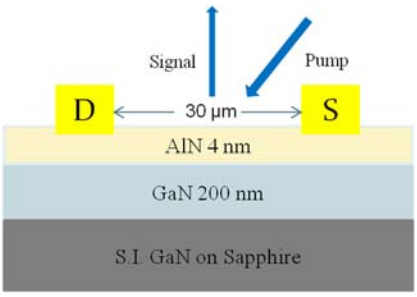

Figure 2.4 GaN HEMT device structure 1.

As shown in Fig. 2.4, The HEMT structure investigated here was grown using molecular beam epitaxy (MBE). It consisted of 200-nm unintentionally doped GaN on 3-μm of semi-insulating GaN, deposited on top of a 300-μm thick sapphire substrate. Then, the GaN layer was capped by a 4-nm thick AlN layer. High-density two-dimensional electron gas was formed within GaN layer next to the GaN/AlN interface. Source and drain Ohmic contacts were constructed by evaporation of gold film followed by annealing. The channel length was measured to by 30 μm in this experiment. At room temperature, the electron sheet concentration was measured to be 2.5×10^{13} cm^{-2}, and electron mobility was 1200 $cm^2/V\cdot s$.

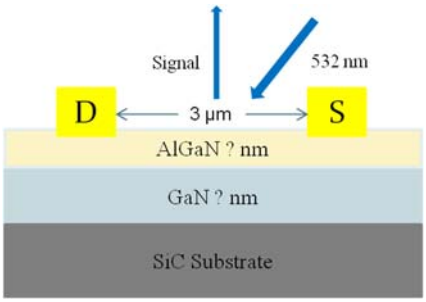

Figure 2.5 GaN HEMT device structure 2.

The sample showing in Fig. 2.5 was a 2nd-generation one used in the DARPA collaboration project. Due to confidential reasons, the sample information and measured data cannot be shown in this dissertation. The Raman shift method was mainly performed on this project using a single grating spectrometer with a long-pass filter and positive results has been achieved. In the next section, we will use data measured from the first sample to illustrate the feasibility of Raman shift method.

Raman signals backward-scattered by the AlN side of HEMT were recorded using a double grating cascaded monochromator at room temperature (295 K) with different bias voltages applied between source and drain in the range of 0-36 V. The Raman signals scattered by monochromator were then measured by a photomultiplier. A 373.9 nm picosecond laser, produced by frequency doubling in a 10-mm thick beta barium borate crystal of mode-locked picosecond Ti:sapphire laser output, was used to excite the sample. The width of each incident pulse was measured to be 3 ps. The power of the laser on sample was set to about 30 mW. The beam was focused down to the HEMT with a beam radius of 150 μm.

IV. Results and Analysis

a. Results from the Raman Ratio Method

As shown in Fig. 2.6 (a) and (b), the Stokes and the Antistokes Raman spectra of the GaN HEMT device were measured under various bias voltages. For Fig. 2.6 (a), the first-order Stokes Raman peaks can be seen on the right side of the spectrum and the second-order peaks can be seen on the left side. While for Fig. 2.6 (b), the first-order Antistokes Raman peaks can be seen on the right side and the second-order peaks can be seen on the left side. The two peaks resolved correspond to the Raman scattering by the LO phonons

in the GaN channel layer, with their phonon energies being $\hbar\omega_{LO} = 91.8\, meV$. Each of the four Raman scattering process is going through its own resonance at a specific electric field.

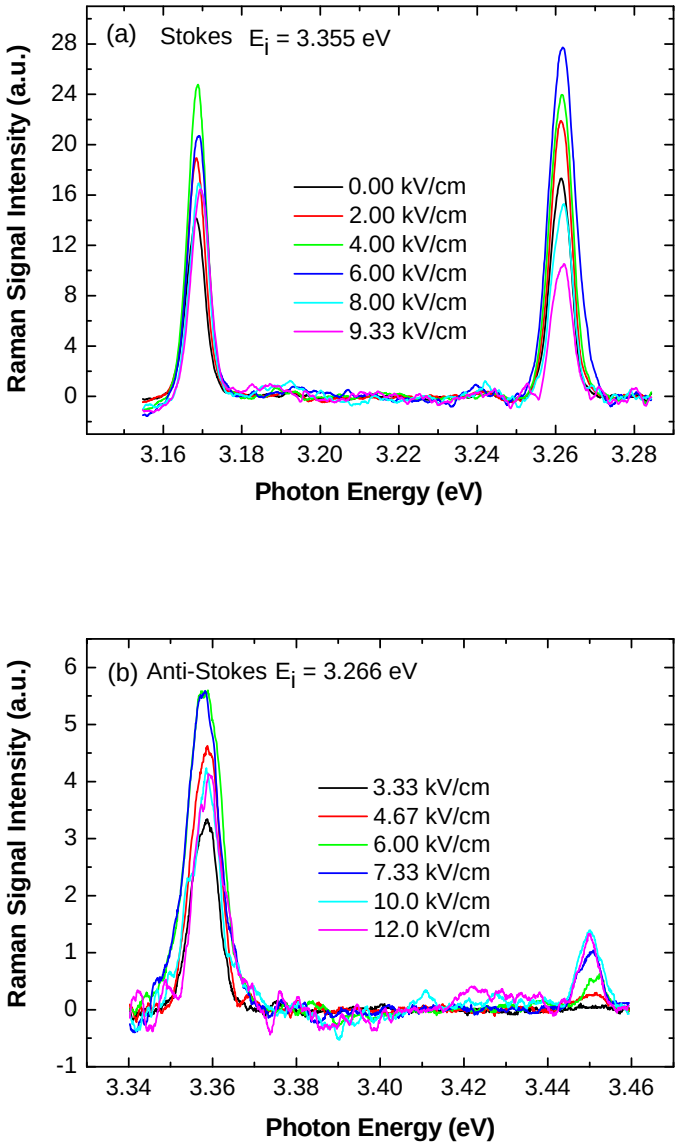

Figure 2.6 Spectra of first-order and second order Raman scatterings at different electric fields as indicated: (a) Stokes (b) Antistokes. E_i is the photon energy of excitation laser. (Figure is from Ref.[2.12])

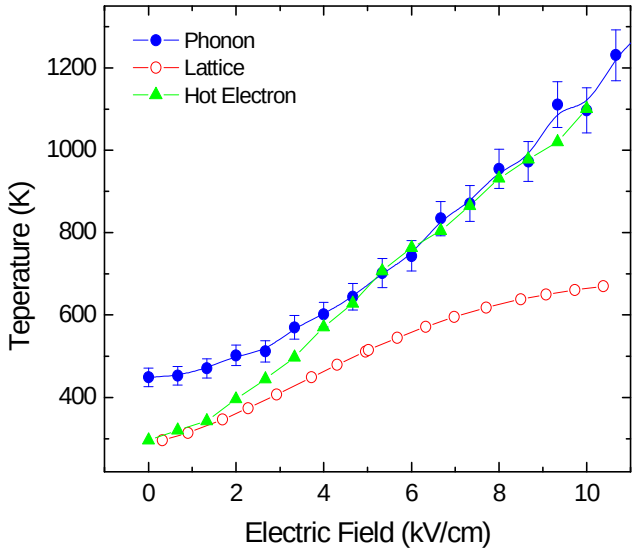

Figure 2.7 Phonon, lattice, and hot electron temperatures at different electric fields. (Figure is reproduced from Ref. [2.11, 2.12])

Using Eq. (4), we were able to determine the phonon temperatures at different electric fields from the first-order Raman scattering, see Fig. 2.7. The phonon temperatures increases almost at the same rate as the lattice temperature for the electric field in the range of 0-5.33 kV/cm. Above 5.33 kV/cm, however, the increase in the phonon temperature is much steeper than that in the lattice temperature. Such a phenomenon implies that in the range of 0-5.33 kV/cm, the increase in the electric field results in the increase of the lattice temperature, and hence the phonon temperature. While above 5.33 kV/cm, the increase in the electric field leads to the generation of extra LO phonons above those determined by the thermal equilibrium at the lattice temperature. These results were published in Ref. [2.11, 2.12]

b. Results from the Raman Shift Method

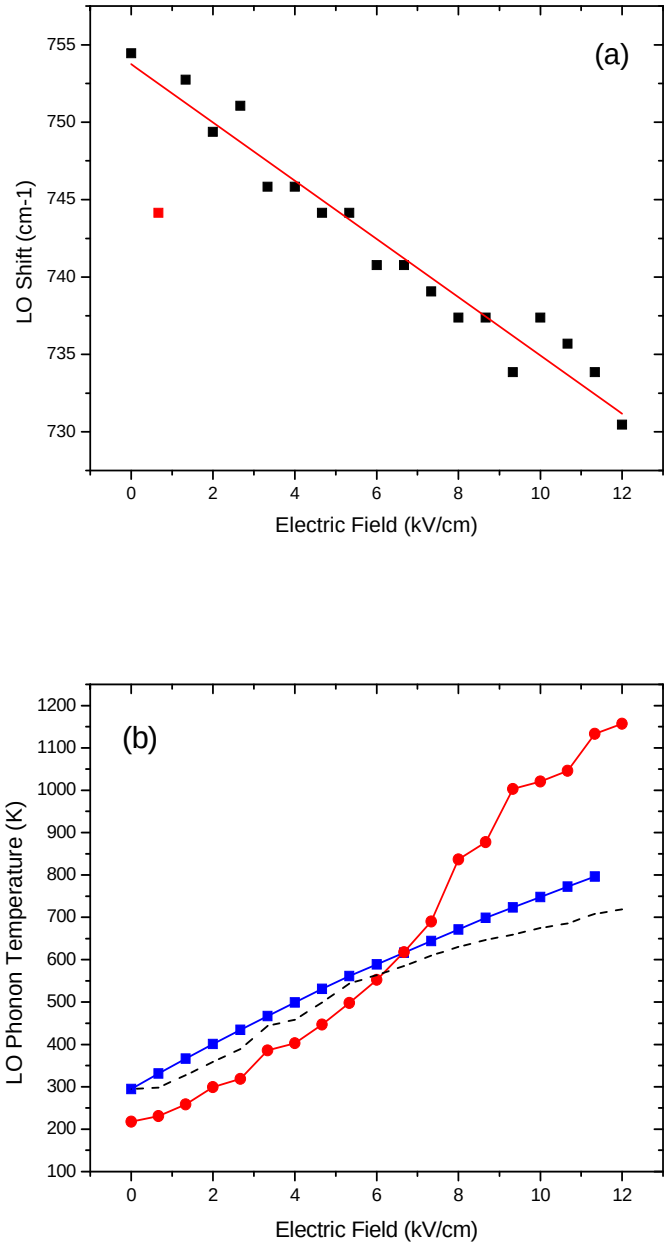

Figure 2.8 (a) LO phonon frequency shift vs. Electric field, experimental data (black squares) and linear fit (red line). One data point (red) is masked for linear fit for large discrepancy. (b) LO phonon temperature, measured by frequency shift (blue squares) and intensity ratio (red circle). Dash line represents lattice temperature.

The measured frequency shift of A_1(LO) of GaN is shown in Fig. 2.8 (a). As one can see, the phonon energy exhibits tendency of continuous red shift while bias voltage increases.

A linear fit for the data points (red line) is feasible for smoothing out the noise with a slope around 16 cm^{-1}/12 kV/cm. Using such linear fit as averaged values of frequency shift, we can recover the LO phonon temperature in operation according to Eq. (7), shown in Fig. 1 (blue squares). The values of $\omega_0, A,$ and B are 763 cm^{-1}, -4.7 cm^{-1}, and -0.01 cm^{-1}, respectively, for our HEMT structure. The thermal expansion coefficients α_c and α_a and Grüneisen parameter γ were taken from Refs. [2.13] and [2.14]. The layer stress part of the model was neglected since the lack of growing conditions of the device.

Clearly, the phonon temperature experienced large increase while bias voltage was tuned up, from room temperature to over 800 K. Meanwhile, the phonon temperature deduced by intensity ration method is also represented in Fig. 2.8 (b) (red circles). This measurement also exhibits phonon temperature increase with rising bias voltage with a larger temperature range, from approximately 200 K to 1200 K. The dash line with hollow triangles represents the changing of lattice temperature. One can observe that above 6 kV/cm, both phonon temperatures are significantly higher than lattice temperature, indicating that hot phonons are generated in the device. This also shows the consistency of the two methods.

Since our sample is measured at room temperature, it is obviously not credible that the data points of intensity ratio method from 0-2 kV/cm are below 295 K. Such divergence from reality is probably introduced from experimental errors. Since anti-Stokes Raman signals are much weaker than Stokes ones, it is difficult to obtain Anti-Stokes Raman spectrum with good quality, which leads to unrealistic temperature in the data. Also, for materials with high-energy phonons such as GaN, measurement of intensity of both Stokes and anti-Stokes modes requires long integration times, which increases the probability of

incident laser power instability affecting the authenticity of intensity ratio, and also makes application of this method unsuitable for fast temperature monitoring. In the range from 2.67-6.67 kV/cm before two curves intersects, both temperatures obtained from two methods are feasible for illustrating LO phonons accumulation in the device. Above 6.67 kV/cm, the temperature acquired from intensity ratio grows much faster than the one deduced from frequency shift. This discrepancy can also be attributed to the fact that anti-Stokes signal intensity is lack of quality.

It is necessary to point out that phonon temperature is a defined term to illustrate the phonon population in the device and hence not a real temperature. Thus, some discrepancy on the absolute values of the temperature can be accepted in our study. The trends of how phonon temperature varies according to the electric field reveals more physical meaning of the behavior of hot phonons in GaN. The eventual goal of this project is to develop a method to monitor the hot phonon behavior in GaN HEMT device operation, and verify the introduction of "isotope disorder" is effective in the reduction of hot phonons in GaN HEMT devices.

V. Conclusions

In conclusion, both methods could reveal the fact that phonon temperature increase with bias voltage, and hot phonons were generated in the process of device operation. However, intensity ratio method requires more experimental complications, including anti-Stokes signal quality, tuning incident laser frequency and long integration time, which may contribute to infidelity of temperature results. Frequency shift method could retrieve

accurate temperature from the device, providing that accurate wavelength resolution is accessible, and preferably temperature-phonon frequency calibration is performed.

One possible way of suppressing the hot phonon effect from deteriorating device operation is to introduce isotope disorder into GaN, which will not fundamentally enhance LO phonon decaying into acoustic modes, but will spread LO phonons around Brillouin zone by increasing the density of LO phonon modes, thus providing more channels for cooling of electrons [2.15]. Theoretical and experimental work based on such a concept is under current investigation.

Chapter 3 Optical Refrigeration by Phonon Assisted Photoluminescence

I. Introduction

The term “optical refrigeration” is also known as “laser cooling”, and the latter is usually referring to the cooling and trapping atoms and ions in the form of dilute gases [3.1]. This area of research made feasible of the observation of Bose-Einstein condensation [3.2]. However, half a century before the achievement of Doppler cooling of atom gas and even the invention of laser, the concept of optical refrigeration of solids through the use of phonon-assisted Antistokes photoluminescence (ASPL) has been already proposed by Peter Pringsheim in 1929 [3.3], see Fig. 1. The physics of this process, unlike its Doppler cooling counterpart, is pretty straightforward, see Fig. 1 [3.4]. First, a light source of photon energy same as the bandgap of solid materials is used as a pump source. The electrons on the ground states of the solid materials will absorb the photon energy, and will be pumped to the exited states. These exited electrons will be all located at the bottom part of the exited states. However, according to the quasi-thermal equilibrium condition, the electrons distribution in the exited states should follow the Fermi-Dirac distribution, which means some of these electrons will be relocated to higher energy states. Such process is fulfilled through the scattering among electrons and the lattice. After the quasi-thermal equilibrium is reached, the average energy of electrons is going to be higher than the bandgap, i.e. the photon energy of the pump source. The energy difference is actually compensated by the lattice vibration energy, i.e. phonon energy through scattering. In the end, the exited electrons will decay to the ground states and emit photons. If all the electrons will lose their

energy through emitting photons, i.e. the luminescence quantum efficiency is 100%, the lattice thermal energy will be extracted from solid materials. Eventually, such solid materials are cooled down by removing phonons.

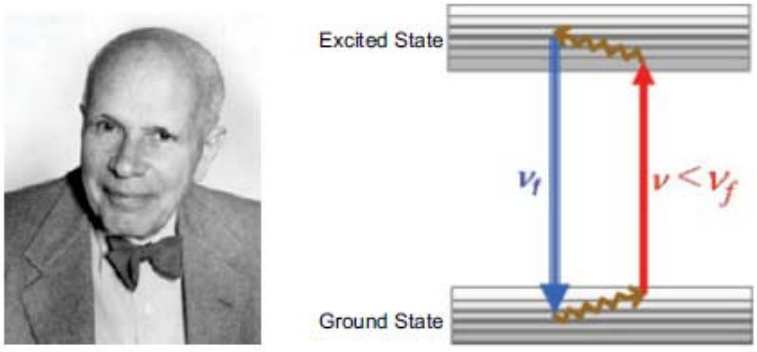

Figure 3.1 Peter Pringsheim (left); A scheme of Antistokes Photoluminescence (right). Figure is reproduced from Ref. [3.4].

The physical picture of optical refrigeration of solids described above leads to the following requirements. First, the Antistokes photoluminescence should be observed during the optical cooling process, i.e. the average fluorescence light frequency ν_f should be larger than the pump light frequency ν_p. Second, if net cooling can be achieved, the quantum efficiency of photoluminescence should be close to unity. A simple estimation would show that the quantum efficiency η_{QE} should be at lease larger than ν_p/ν_f. The typical quantum efficiency of solids in optical cooling experiments would be higher 97%. Third, assuming the quantum efficiency is 1, the cooling efficiency of fractional cooling energy for each electron, i.e. η_C is equal to $(\nu_f-\nu_p)/\nu_p$. In thermal equilibrium, $h(\nu_f-\nu_p)/h\nu_p = k_BT/h\nu_p$. Assuming $h\nu_p$ is around 1 eV, the cooling efficiency would be less than 5%.

Since it is not after the invention of laser in the 1960s, the early research of optical refrigeration is merely focused on the feasibility of the principle. It way initially believed

that the Antistokes cooling theory would contradict the second law of thermodynamics. The cycle of excitation and fluorescence was predicted to be a reversible process, and hence the optical refrigeration would be the same as the complete transform from heat to work [3.5, 3.6]. Such dispute was closed by Landau by assigning entropy to light radiation [3.7]. In his paper, the entropy of radiation field increase with its bandwidth and also the solid angle through which it propagates. Thus, if the pump beam has a minimum bandwidth and a defined propagating direction, it would have almost zero entropy. Such requirements would only be perfectly fulfilled by laser. On the other hand, the fluorescence light has a much broader bandwidth and is radiated in all directions. Thus, it would have larger entropy comparing to the pump laser. The second law of thermodynamics wouldn't be violated with such process.

The experimental efforts of development on optical refrigeration has begun after the invention of laser, but the requirement of extremely high fluorescence quantum efficiency put the observation of net cooling on hold for decades. Until 1995, the first experiment demonstration of laser cooling was realized by Epstein *et al*. with ytterbium-doped fluorozirconate glass, i.e. ZBLANP:Yb^{3+} [3.8]. Nowadays the rare-earth doped material technology of laser cooling has approached cryogenic temperatures, and, efficiency-wise, already has beaten the performance of typical thermoelectric coolers [3.9]. The potential applications of optical refrigeration include the cooling of satellite instrumentation and small sensors, where compactness, ruggedness, and the lack of vibrations is important. The advantages of optical refrigeration are free of moving parts and long operation time.

The optical cooling technology based on rare-earth doped insulating crystal is well developed. However, it is not a practical system -- it is the active semiconductor device

that requires cooling in the end. To reach cooling by attaching the rare-earth doped crystal to the semiconductor devices, there are major issues including low thermal conductivity of rare-earth host materials and the inferior thermal contact between the crystals and the semiconductors. It would be desirable to have laser cooling implemented directly with semiconductor material for simpler integration of cooling and active devices. Moreover, the potential extreme cooling temperature can reach down to ~ 10 K with semiconductors [3.10, 3.11], which may not be achieved by rare-earth doped crystals since the severe depopulation of the top of the ground states of rare-earth ions at such low temperature. Semiconductors are free of such problem since the valence band is always populated with electrons.

The advantages of semiconductors for laser cooling are obvious, and thus the field of study has been investigated intensively both in theory and experiment [3.10 – 3.18]. There was considerable amount of effort spent on the material of GaAs, since its technology is the most mature one among the direct bandgap semiconductors. Also, an external radiative recombination efficiency over 96% has been observed in a GaAs/InGaP heterostructure [3.19]. As mentioned before, the radiative efficiency is a key factor of realizing laser cooling. In each cooling cycle of Antistokes photoluminescence emission, only about $k_B T$ of energy is being taken away, which is about 1% of the pump photon energy. Hence, non-radiative recombination loss of merely 1% would be fatal for laser cooling. Till now, no net cooling has been achieved with GaAs despite all the attractive features aforementioned.

Unexpectedly, the first observation of laser cooling using semiconductor was recently attained in CdS nanobelts [3.20]. In the paper, the author suggested that the strong exciton-longitudinal optical (LO) phonon coupling through Fröhlich interaction played an essential

role in realizing optical cooling in semiconductors. Such interaction is the dominating mechanism for Antistokes photoluminescence in polar semiconductors, like GaAs and CdS [3.15]. Thus, comparing with III-V semiconductors such as GaAs, more polar II-V semiconductors, like CdS, are believed to generate more efficient ASPL since their Fröhlich interaction is stronger. Another argument of why CdS is in favor of GaAs on laser cooling is its larger bandgap (2.4 eV vs 1.5 eV). The prospects of laser cooling using other II-IV materials were also discussed [3.21]. The larger bandgap leads to the facts of large joint density of states, lower refractive index, and very low Auger recombination rate, which are all advantageous for laser cooling [3.16]. To compare on factors including bandgap and strength of Fröhlich interaction among potential semiconductor materials in Table 3.1.

Table 3.1 Bandgap and Frohlich coupling constants of several semiconductors (see Ref. [3.22]).

System	Materials	α_F	E_g (eV)
IV	Si	0	1.12
III-V	GaN	0.48	3.4
	GaP	0.201	2.26
	GaAs	0.068	1.424
	InP	0.15	1.344
II-VI	CdSe	0.46	1.49
	CdS	0.51	2.5

The Fröhlich constant α_F represents the strength of coupling between electron and LO phonon. As we can see from Table 3.1, the materials in the II-VI group overall have larger Fröhlich constants than the ones in the III-V group. Indeed, comparing GaAs and CdS, the former has a Fröhlich constant of only 0.068 and the latter has one of 0.51 [3.22]. However, one materials in the III-V group stands out in the category of α_F is GaN. With an α_F of 0.48,

almost the same as that of CdS, and also a significantly large bandgap of 3.4 eV, GaN would potentially be a favorable candidate for investigating laser cooling. Indeed, GaN contains many attractive properties, including large LO phonon energy (~90 meV), high joint density of states (less saturation), wide bandgap (weak Auger recombination), and small refractive index (less light trapping). Also, with the mature technology of GaN and its alloys (e.g. AlN, InN) developed in growth, fabrication, and light extraction along the populated application in both electronics (high speed and high power transistors [3.23]) and photonics (LEDs and laser diodes [3.24]), it is obvious the time to commence experimental works on the development of laser cooling using GaN material.

In this chapter, we report our investigation of Antistokes photoluminescence of free-standing GaN and GaN nanowire material. The strong light emission we measured gave us the confidence to believe that laser cooling may be achieved with GaN in the near future.

II. Sample Description and Experimental Setups

The sample we used in our experiments is a free-standing GaN wafer and a GaN nanowires sample. The free-standing GaN wafer was grown by metal organic chemical vapor deposition (MOCVD) with Si donor concentration of 2×10^{18} cm^{-3}. The nanowire sample is made of catalyst-free GaN nanowires grown directly on a Si (111) substrate under nitrogen rich conditions by radio frequency plasma-assisted molecular beam epitaxy (MBE). The area density of the nanowires was estimated to be $\sim1\times10^{10}$ cm^{-2}. The samples were mounted on a cold finger of a-continuous-flow cryostat with its temperature being set from 4.2 K to 475 K. The pump light source was a Ti:sapphire laser with a 3 ps pulse length, a repetition

frequency of 76 MHz and a wavelength tunable from 730 nm to 850 nm. The laser pulse was subsequently either frequency doubled or quadrupled by using either one or two BBO crystals, which allowed the excitation of GaN either across or above the bandgap. The focal spot of the pump beam on GaN samples is typically 0.02 mm^2. For the free-standing GaN sample, the photoluminescence (PL) signal was collected by a double-grating spectrometer; while for the GaN nanowire sample, the PL signal was collected by a single-grating spectrometer, with appropriate filters to block the strong laser signal before the light enters it. The spectral analyzed light was detected by a photomultiplier tube.

III. Results and Discussions

We first measured the PL spectra using free-standing GaN sample with pump photon energy well above the bandgap of GaN, i.e. a 209 nm laser source generated with 2 BBO crystals for frequency quadrupling from a Ti:Sapphire laser. The average pump power was 0.5 mW. The PL spectrum of GaN obtained at 6 K is shown in Fig. 3.2. The dominant peak located at 357.3 nm corresponds to the recombination of the excitons bound to neutral donors (D-X or I_2) whereas a small peak around 368.13 nm is caused by recombination of electrons bound to the donors with free holes (D-h). The three peaks at 380.08 nm, 390.96 nm, and 402.49 nm correspond to the recombination of the donor-acceptor pairs (DAP) and its 1LO-phonon and 2LO-phonon replicas, respectively. The strong intensities of LO-phonon replica of DAP indicate the strong coupling between electrons (or holes) bound to donors (or acceptors) and LO phonons. When the sample temperature is increased, the peak

of DAP progressively evolves towards the exciton peek, as also shown in Fig. 3.2, and eventually, above 200 K all the sharp features in the spectrum disappear.

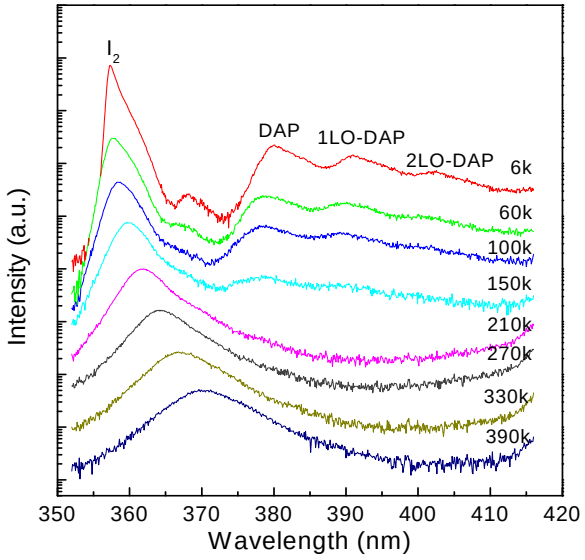

Figure 3.2 PL spectra excited by 209 nm laser with an average power of 0.5 mW under different temperatures.

We then move closer to the investigation of optical refrigeration by exciting the sample with pump photon energy below the bandgap. The ASPL spectra of free-standing GaN are shown in Fig. 3.3. The red curve of Fig. 3.3 shows a typical ASPL spectrum measured at 385.6 nm at room temperature. The dominate ASPL peak is 71 meV above the pump photon energy, well above $k_B T$, while the LO phonon energy of GaN is 92 meV, only slightly larger than the difference mentioned above. Such phenomenon is in full agreement with results shown in Ref. [3.15]. From the analysis above, the ASPL process can be understood with the following 3 steps: first, the pump photon was absorbed with the assistant of LO-phonon; second, the exited electrons in conduction band went through thermal equilibrium, with the releasing of acoustic phonons carrying away about 21 meV of energy to the lattice; finally, the electrons recombined with the holes directly and

radiated photoluminescence, which does not involve phonons in this step. The 71 meV energy difference between ASPL main peak and pump photon energy also clarify the fact that what we observed was ASPL rather than AS Raman, since the latter always has a shift equal to the phonon energy.

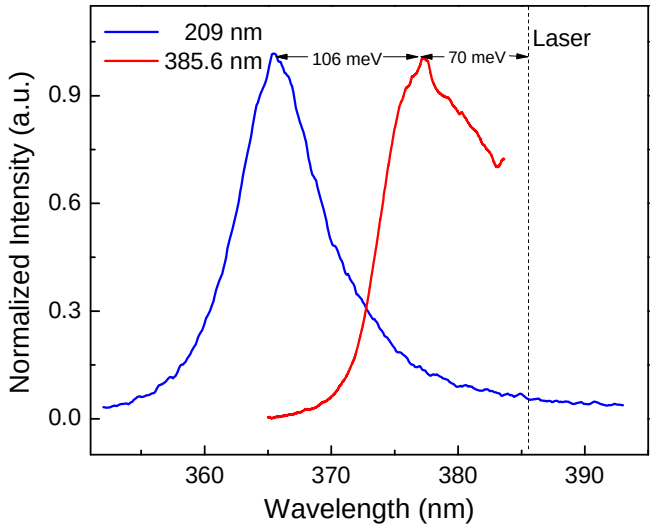

Figure 3.3 Normalized PL spectra measured at 300 K at the excitation wavelength of 209 nm (blue curve) and 385.6 nm (red curve).

We also took a comparison between the PL obtained while pumping well above the bandgap and ASPL acquired by pumping below the bandgap, as showed in blue and red curve in Fig. 3.3, respectively. The above bandgap PL peak is about 106 meV higher than the ASPL peak, indicating that the absorption when pump below the bandgap is relatively weak such that the states above bandgap was not filled up. In such case, the ASPL was originated from the states below the nominal bandgap, which is called the "Urbach tail" [3.26]. It was stated in Ref. [3.26] that there are still states available below the bandgap,

with the density of states decaying in exponential rate while stepping away from the bandgap. These Urbach tail states are advantageous for laser cooling since the electrons can temporarily reside on them after pumped by incident laser, while waiting for the assistance of LO phonons to "climb up" to the conduction band [3.15]. Thus, in the purpose of cooling, the semiconductor should be excited below the nominal bandgap into the Urbach tail. The origin of these tail states can be either extrinsic (defect/impurities) or intrinsic (phonon assisted absorption) nature. The extrinsic Urbach tail might be less suitable to be used for laser cooling, since such ASPL process is always accompanied with background absorption. Though this origin unknown background absorption is very weak, it would be seriously obstacle to cooling (As we stated in the introduction section, non-radiative recombination of merely 1% would be fatal for cooling). It is also studied in Ref. [3.14] that the donor-acceptor transition below the bandgap can be used for laser cooling. The cooling threshold was found to be lower though, the cooling power was found to be very weak due to the saturation of the donor-acceptor transition. Meanwhile in concept, it is not that different from the usage of extrinsic Urbach tail.

On the other hand, the intrinsic Urbach tail – the one results from phonon-assisted absorption appears to be a natural choice for the purpose of laser cooling. Such tail states almost ensured the production of strong Antistokes shift in PL, since the joint density of states in the conduction band (which is above the pump photon energy) is always larger than the density of states in the tail. In Ref. 10 the author investigated the potential of utilizing intrinsic Urbach tail for laser refrigeration and showed than although the phonon assisted absorption does get saturated, it usually happens at relatively high pump powers. The author also showed that another process of phonon-assisted electron-hole

recombination (the reverse process of phonon-assisted absorption) also occurs, which results in a Stokes shifted photoluminescence not in favor of the cooling purpose. However, by properly choosing the excitation wavelength, one can make sure that the Antistokes PL dominates, as was indeed observed in our experiments. The fact that phonon-assisted absorption resulted Urbach tail usually exists in high purity semiconductor material is specially favorable of laser cooling, since in high purity materials the rate of background absorption, which deteriorates the cooling purpose, can be ignored.

Evidently, the potential of optical refrigeration becomes promising when the depth and strength of Urbach tail are enhanced. The depth of Urbach tail, i.e. how far the exponential states extends below the bandgap, is determined by the energy of LO phonons. The strength of phonon-assisted absorption, on the other hand, is proportional to the electron-phonon interaction strength, i.e. Fröhlich interaction, which is especially strong in polar semiconductors. With the analysis above, GaN can be an outstanding choice for the investigation of laser cooling, not only since its very large LO phonon energy stands out among its competitors (92 meV for GaN, 36 meV for GaAs, 37 meV for CdS), but also since its large Fröhlich constant (0.48 for GaN, 0.51 for CdS, 0.07 for GaAs).

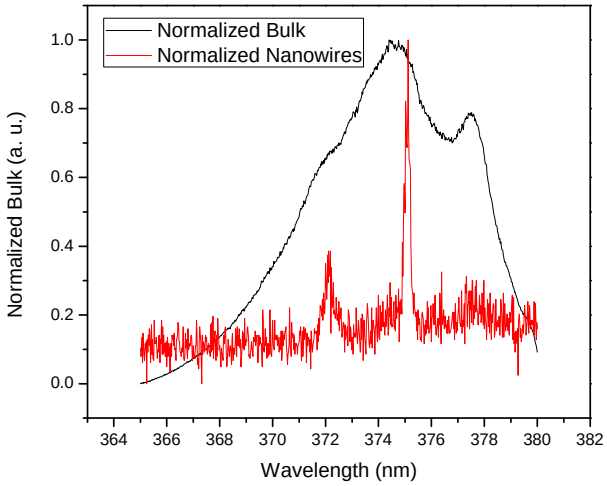

Figure 3.4 Comparison of normalized ASPL signals of freestanding bulk GaN (black curve) and GaN (red curve) nanowire samples at room temperature.

For the measurement of GaN nanowire sample, We chose the pump laser wavelength was set at 382.8 nm with power of 20 mW, because it is roughly 1 LO phonon energy below the ASPL emission peak wavelength from the free-standing GaN sample, also because this is the shortest wavelength for a 390 nm short-pass filter to sufficiently suppress the pump laser so that the ASPL signal won't be covered by the tail of strong pump laser, with the limited resolution provided by the single grating monochromator. The red curve in Fig. 3.4 showed that at room temperature, we could barely detect any photoluminescence signals, while two sharp peaks of Raman scattering by the GaN TO and LO phonons could be easily identified. The stronger peak at 375.3 nm is due to the Antistokes Raman Scattering of E_2 TO phonons with a phonon energy of 64.7 meV, while the small bump at 372.3 nm is due to the A_1 LO phonons with a phonon energy of 91.3 meV. Such a phenomenon distinguished obviously from the one we measured on a bulk freestanding GaN sample, as

shown with black curve in Fig. 3.4, which presented a clear broad PL peak at 374.6 nm and no Raman narrow peaks. The weaker peak at 377.5 nm was due to the edge of the short-pass filter. Since the intensity of ASPL from GaN nanowires sample was more than 100 times smaller comparing to the one from bulk GaN sample, both of the curves were normalized for a clear illustration. This indicated that for the GaN nanowire sample with much smaller area density of active media than the bulk GaN, we might need a higher temperature or a pump photon energy closer to the GaN bandgap to boost up the radiative recombination rate, hence the intensity of the PL. Since there is no suitable short-pass filter for any shorter pump wavelength, we chose to increase temperature. The bandgap would also shift to lower energy with the increase of temperature [3.25], which brings the pump laser closer to the bandgap, and hence increase the absorption rate. Indeed, when the temperature increased, we could observe the enhancement of the ASPL signal, as shown in Fig. 3.5. We could see that at 350 K, both Raman signals from TO and LO phonons increased. And at 400 K, a significant contour of PL signal was present underneath the two Raman peaks. Especially at 475 K, the Raman peaks were completely insignificant, indicating that the major signal detected at such temperature is the ASPL. The main PL peak at 475 K locates at the wavelength of 373.5 nm, which is a 80.6 eV blue shift of the pump laser photon energy. Also, as temperature increased, the intensity of PL signal enhanced dramatically. Comparing the height of PL contour at 300 K and the one at 475 K, the enhancement is more than one order of magnitude.

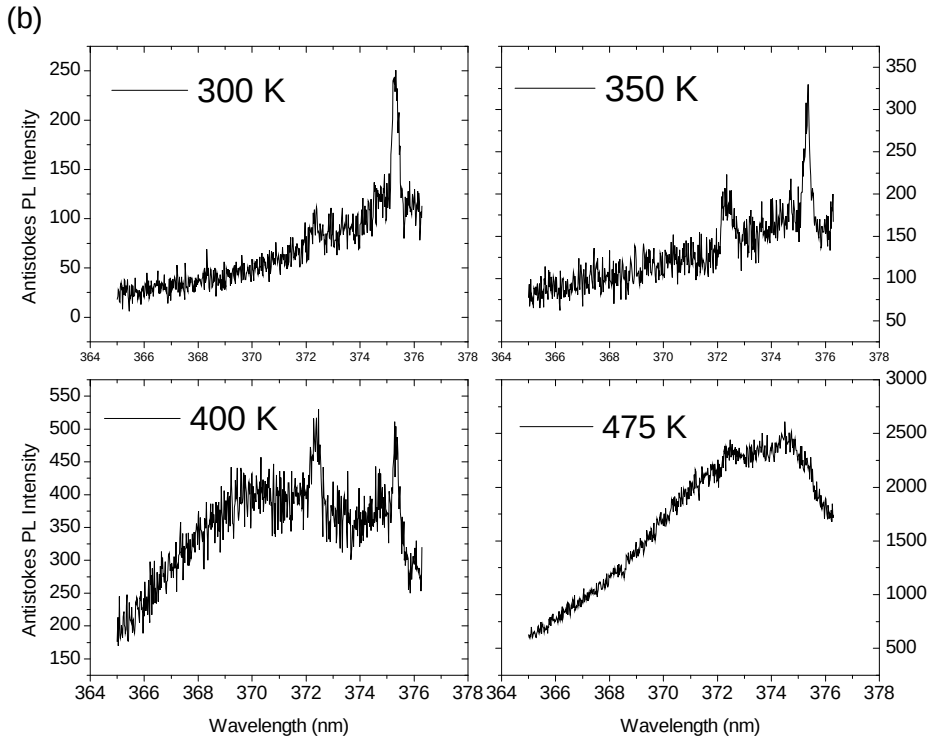

Figure 3.5 ASPL signal of GaN nanowire sample measured at the temperature of 300 K, 350 K, 400 K, and 475 K.

To confirm that the ASPL we measured in both free-standing GaN and GaN nanowire is indeed induced by phonon assisted absorption, we have measured the intensity of ASPL in the dependence of its pump power. Besides ASPL induced by phonon assisted absorption, luminescence upconversion in semiconductors can also be the result of two-photon absorption [3.28]. Since there are two photons involved in one upconversion cycle, the intensity of ASPL resulted from two photon absorption should be proportional to the square of pump power. On the other hand, since only one photon is needed in the cycle of phonon-assisted absorption, the power dependence of phonon-assisted ASPL should be a linear relation. As we can see in Fig. 3.6 (a), at the excitation wavelength of 386.5 nm, up to the pump power of 40 mW, the integrated intensity of ASPL from free-standing GaN sample

is proportional to the pump power. In comparison, we also measured the dependence using a CW laser pumping the free-standing GaN sample at the wavelength of 532 nm, which is far below the bandgap of GaN. The ASPL generated with 532 nm excitation, as shown in Fig. 3.6 (b), has intensities proportional to the square of pump power. Note the fact that the intensity of PL excited by 385.6 nm wavelength is at least four orders of magnitude higher than that for the two-photon absorption induced PL.

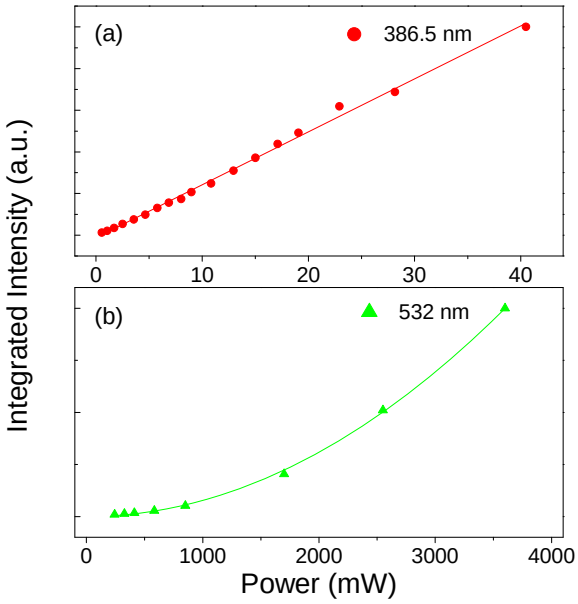

Figure 3.6 Integrated PL intensity of freestanding GaN as a function of pump laser power measured at room temperature: (a) excited at 385.6 nm. (b) excited at 532 nm. The solid red and green lines are linear and quadratic fitting, respectively.

To further support our analysis, for the GaN nanowire sample, we also measured the intensity of ASPL as a function at 475 K, with an excitation wavelength of 382.8 nm, see Fig. 3.7. It is obviously illustrated that up to the pump power of 50 mW, the intensity of ASPL increased linearly with the excitation power. Such a phenomenon also supports the fact that when GaN nanowires was exited at the phonon energy being roughly 1 LO phonon energy lower than the bandgap, the ASPL was induced by one photon absorption process.

The energy difference between pump photon and PL emission was made up by the energy of LO phonons. Unlike the bulk GaN sample, since the recombination rate of nanowires were much smaller, the linearly scaling up behavior of ASPL with pump power could only be observed at elevated temperatures.

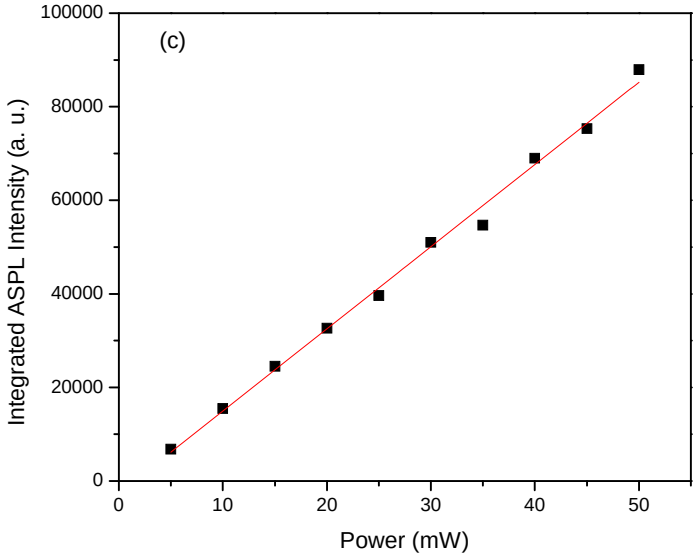

Figure 3.7 Integrated ASPL intensity of GaN nanowire sample as a function of pump power measured at the temperature of 475 K. Square dots are experimental results, red curve is a linear fit.

When we tune the excitation wavelength from 385 nm to 410 nm, we observed the nearly exponential decrease of ASPL intensity, as shown in Fig. 3.8 (a). Such fact was predicted in Ref. [3.15]. One can observe the transition from the phonon-assisted process to two-photon absorption process in the behavior of ASPL. The exponential trend is still persistent when the pump photon energy is more than 1 LO phonon energy below the bandgap, suggesting the fact that the absorption phonon assistance process gradually evolve from involving one phonon to two phonons. The similar trend was discovered by other groups on the ASPL experiments of CdSe quantum dots [3.21] and GaAs quantum wells [3.17].

However, when the pump wavelength is beyond 400 nm, the intensity of ASPL stop decreasing and almost stays as a constant. Such a trend indicate that the two photon absorption process is stronger than the weak phonon-assisted absorption involving three or more phonons. To verify the assumption that the ASPL gradually changes from phonon-assisted to two photon absorption while the pump wavelength moving away from bandgap, we have measured the pump power dependence of ASPL intensity at several excitation wavelengths. Indeed, we can see in Fig. 3.8 (b) that while the pump wavelength shifts from 382.1 nm to 409.1 nm, the dependence

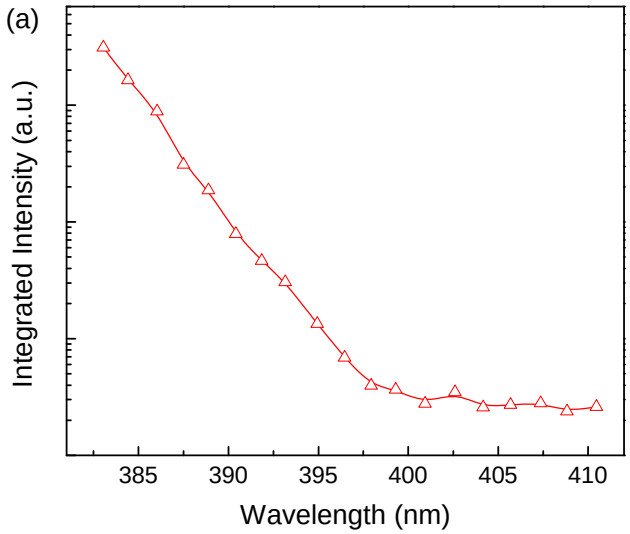

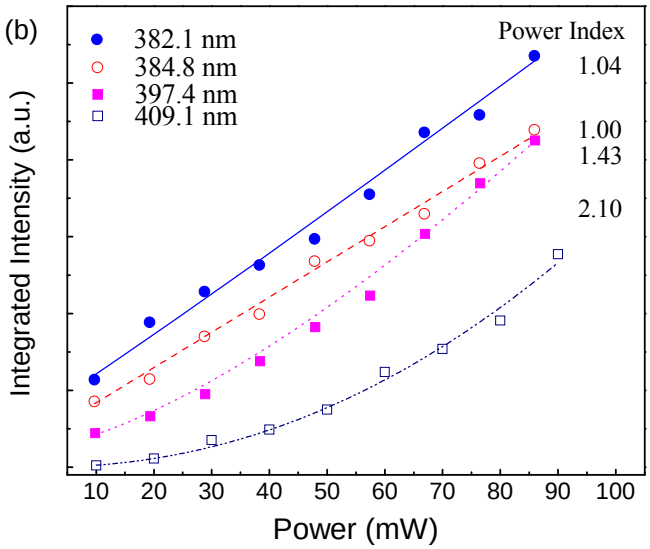

Figure 3.8 (a) Integrated PL intensity as a function of excitation wavelength measured at the temperature of 300 K. Pump power is set as 20 mW, the solid line is guide for eye. (b) Integrated PL intensity as a function of pump power at four different excitation wavelengths measured at room temperature. The curves show the fitting of experimental data by the function of $I \sim P^{\alpha}$, where I is the integrated PL intensity, P is the pump laser power, and α is the power index.

of ASPL intensity on pump power gradually evolves from linear to quadratic. The two-photon absorption process inclines to heat up the sample instead of cooling it down, so it would be better to reduce this effect. Thus, a CW laser excitation should be used in the cooling experiment rather than a pulsed one, just as the one with succeeded cooling on CdS [3.20].

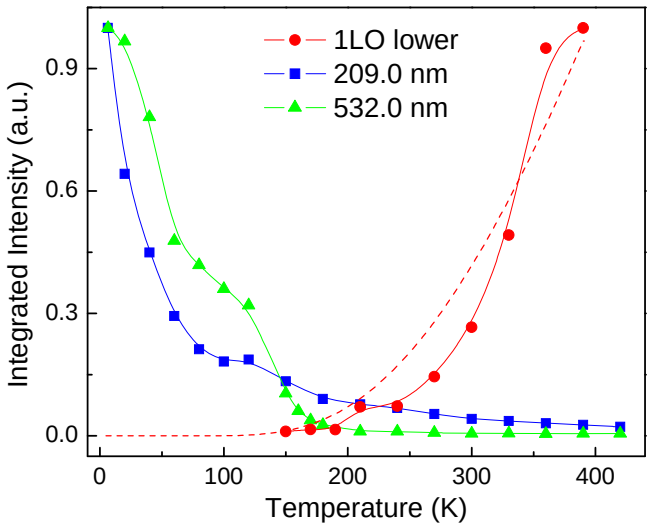

Figure 3.9 Normalized integrated PL intensity as a function of temperature at different excitation wavelengths. The solid lines are guide for eye. The dashed line indicates the Bose-Einstein statistics, assuming that intensity of ASPL is proportional to the number of LO phonons.

It is possible that the ASPL intensity increases with temperature rising would be the clearest indication of phonon-assisted process [3.21]. As it is shown in Fig. 3.9, the intensity of ASPL scales up dramatically with the ramping up of temperature from 150 K to 390 K. Similar behavior was also observed in our GaN nanowire sample measurements, as can be seen in Fig. 3.5. Since the intensity of ASPL is very sensitive to the selection of pump wavelength, see Fig. 3.8 (a), in this measurement the excitation wavelength is tuned to keep its photon energy always approximately 1 LO phonon energy lower than the emission peak of ASPL. The data below 150 K cannot be shown since the ASPL signal strength is significantly diminished and overwhelmed by the laser tail, given limitations of our experimental setup. The dependence of ASPL intensity on temperature obeys the trend of Bose-Einstein distribution, as shown by the dashed curve in Fig. 3.9, suggesting that the ASPL is induced by a one phonon assisted process. To compare with PL signals excited at

other wavelengths, we measured the dependence of PL signal strengths to pump power at both wavelength of 209 nm and 532 nm, i.e. well above and well below the bandgap energy, respectively. In both these cases, the electrons are excited directly well above the conduction band bottom by either one photon or two photon absorption, without the assistance of phonons. As shown in Fig. 3.9, the PL intensities excited by these two wavelengths are decreasing with the rising of temperature, which is most possibly the results of increased nonradiative recombination. The temperature behavior of ASPL in GaN freestanding sample and GaN nanowire sample both supports the fact that the upconversion observed in our experiments is assisted by LO phonons.

IV. Conclusion

In summary of the chapter, we have observed ASPL from both GaN freestanding sample and GaN nanowire sample. The mechanism of ASPL has been attributed to phonon-assisted upconversion, which can be used to achieve optical refrigeration, with measurements evidence from the dependence on both pump power and temperature. Indeed, the observation of phonon-assisted ASPL is merely the first step of the investigating of cooling, we believe that our results give us confidence on the prospect for using GaN as the base material of semiconductor laser cooling.

Chapter 4 Summary and Outlook

In this chapter, we briefly summarize our work through the chapters and provide outlook directions for possible future research.

In Chapter 1, we studies the backward THz generation through optical rectification using periodically poled $LiNbO_3$ and $LiTaO_3$ (PPLN and PPLT, respectively). The enhancement of THz output powers in both materials were attributed to the enhance second-order nonlinear coefficient due to transverse-optical (TO) phonon polariton resonance. With the PPLN sample, we have generated the shortest wavelength of 62.5 μm at the poling period of 7.1 μm, and also observed an output enhancement as large as 61 times. The polariton resonance at 40 μm is the root of this enhancement. With the PPLT sample, we have generated the largest output power close to 100 μW. A polariton resonance at 78.7 μm was predicted through the least square fit of effective second-order nonlinear coefficients. Such a resonance can be generated by beating two TO phonons of LiTaO3, due to its strong anharmonicity in the phonon Hamiltonians. To verify our prediction, another wafer of PPLT of much shorter poling period was designed for test. We have observed the complete resonance.

Possible future research directions of this topic can be conducted in the following: first, build a better theoretical model to consider all effects originated from the polariton resonance, such as nonlinear coefficient enhancement, absorption enlargement, index change and its effect on THz power extraction, etc. to find out the ultimate wavelength range for maximum output power. Second, a new scheme of surface emitting THz generation can be implemented, since it is the best way to maximum the nonlinear interaction length and minimize THz absorption.

In Chapter 2, we investigated on the hot phonon behavior in GaN HEMT device. A phonon temperature was defined to quantitize the phonon population, and two measurement method was proposed. The first method makes extraction of phonon temperature through the ratio of intensities between Anti-stokes and Stokes Raman signal. It requires more complexity in experimental efforts, which may lead to errors in temperature measurements. The second method obtain the temperature through fitting the Stokes Raman peak shift to a model. It is simple in experimental facilitations, however needs multiple parameter inputs depending on material properties. A proper calibration of the model is necessary for more accurate fitting of the temperature. The ultimate purpose of our project is to develop an accurate and effective method to experimentally measure the phonon population in both regular and isotope doped GaN HEMT samples and verify if the latter has reduce hot phonon numbers as predicted in theory.

If future research would be conducted on this problem, one would suggest to develop a better theoretical model based on experimental data of the second order Raman signals, since they would contain information from all electron-phonon collisions in the entire momentum space. One would also suggest the usage of tunable CW laser of output photon energy near the bandgap of GaN for narrowband Raman signal output and a spectrometer with triple grating to eliminate the necessity of filters and to have more accurate measurement of Raman peak positions.

In Chapter 3, we have studied the photoluminescence upconversion of both free-standing bulk GaN and GaN nanowires on silicon substrate. We have proved experimentally that the PL upconversion we observed was generated through one-photon

phonon-assisted process, through the dependences of PL densities to excitation power, incident wavelength, and temperature. Such upconversion process can be exploited for optical refrigeration in semiconductors.

Further research on this project shall be not only focus on growing high purity GaN material to maximize emission quantum efficiency and minimize non-radidative recombination, but also on more detailed theoretical study of how bandgap energy, phonon energy, and Fröhlich interaction strength affect phonon removal rate and hence cooling efficiency.

In the end, we would like to point out that the research of this dissertation in not only on the purpose of each individual area, but also on the effort to explore more applicable techniques that can be developed into applications through the studies of photon-phonon interaction.

References

[0.1] Y. J. Ding, J. Opt. Soc. Am. B.**28**, 997 (2011).

[0.2] X. Lin, L. Wang, Y. J. Ding, "Efficient generation of far-infrared radiation in the vicinity of polariton resonance of lithium niobate," Opt. Lett. **37**, 3687, (2012).

[0.3] R. Chen, G. Sun, G. Xu, Y. J. Ding, and I. B. Zotova, "Generation of high-frequency terahertz waves in periodically poled $LiNbO_3$ based on backward parametric interaction," Appl. Phys. Lett **101**, 111101 (2012).

[0.4] R. Chen, G. Xu, G. Sun, and Y. J. Ding, submitted to J. Opt. Soc. Am. B.

[0.5] G. Xu, X. Mu, Y. J. Ding, and I. B. Zotova, Opt. Lett. **34**, 995 (2009).

[0.6] A. Link, K. Bitzer, W. Limmer, R. Sauer, C. Kirchner, V. Schwegler, M. Kamp, D. G. Ebling, and K. W. Benz, J. Appl. Phys. **86**, 6256 (1999).

[0.7] S. Choi, E. R. Heller, D. Dorsey, R. Vetury, and S. Graham, IEEE Trans. Electron Dev. **60**, 1898 (2013).

[0.8] A. Sarua, H, Ji, M. Kuball, M. J. Uren, T. Martin, K. P. Hilton, and R. S. Balmer, IEEE Trans. Electron Dev. **53**, 2438 (2006).

[0.9] R. Chen, G. Sun, Y. J. Ding, and J. B. Khurgin, in Proc. of CLEO:2014, San Jose, CA, USA, June 2014.

[0.10] R. I. Epstein, M. I. Buchwald, B. C. Edwards, T. R. Gosnell, and C. E. Mungan, Nature **377**, 500 (1995).

[0.11] M. Sheik-Bahae, and R. I. Epstein, Laser & Photon. Rev. 3, **67** (2009).

[0.12] D. V. Seletskiy1, S. D. Melgaard1, S. Bigotta, A. D. Lieto, M. Tonelli, and M. S. Bahae, Nature Photon. **4**, 161-164 (2010).

[1.1] B. Ferguson, and X-C. Zhang, "Materials for Terahertz Science and Technology", *Nature Materials* **1**, 26 (2002).

[1.2] M. Tonouchi, "Cutting-edge Terahertz Technology", *Nature Photonics* **1**, 97 (2007).

[1.3] G. A. Mourou, C. V. Stancampiano, A. Antonetti, and A. Orszag, "Picosecond microwave pulses generated with a subpicosecond laser-driven semiconductor switch", *Applied Physics Letters* **39**, 295–296 (1981).

[1.4] K. H. Yang, P. L. Richards, and Y. R. Shen, "Generation of Far-Infrared Radiation by Picosecond Light Pulses in $LiNbO_3$", *Applied Physics Letters* **19**, 320 (1971).

[1.5] R. Kohler, A. Tredicucci, F. Beltram, H. E. Beere, E. H. Linfield, A. G. Davies, D. A.

Ritchie, R. C. Iotti, and F. Rossi, "Terahertz Semiconductor-heterostructure Laser" *Nature* **417**, 156 (2002).

[1.6] B. S. Williams, "Terahertz Quantum-cascade Lasers" *Nature Photonics* **1**, 517 (2007).

[1.7] H. J. Bakker, S. Hunsche, and H. Kurz, "Observation of THz Phonon-polariton Beats in $LiTaO_3$", *Physical Review Letters* **69**, 2823 (1992).

[1.8] H. J. Bakker, S. Hunsche, and H. Kurz, "Coherent Phonon Polaritons as Probes of Anharmonic Phonons in Ferroelectrics", *Reviews of Modern Physics* **70**, 523 (1998).

[1.9] M. Bass, P.A. Franken, J. F. Ward, and G. Weinreich, "Optical Rectification", *Physical Review Letters* **9**, 446 (1962).

[1.10] Y. J. Ding, J. B. Khurgin, "A new scheme for efficient generation of coherent and incoherent submillimeter to THz waves in periodically-poled lithium niobate", *Optics Communications* **148**, 105 (1998).

[1.11] Y. J. Ding, "Efficient generation of high-power quasi-single-cycle THz pulses from single infrared beam in second-order nonlinear medium," *Optics Letters* **29**, 2650–2652 (2004).

[1.12] Y. J. Ding, "Quasi-single-cycle THz pulses based on broadband phase-matched difference-frequency generation in second-order nonlinear medium: high output powers and conversion efficiencies", *IEEE Journal of Selected Topics in Quantum Electronics* **10**, 1171–1179 (2004).

[1.13] E. D. Palik, *Handbook of Optical Constants of Solids* (Academic, 1985), pp. 695–702.

[1.14] G. Xu, X. Mu, Y. J. Ding, and I. B. Zotova, "Efficient generation of backward terahertz pulses from multiperiod periodically-poled lithium niobate", *Optics Letters* **34**, 995–997 (2009).

[1.15] O. Eknoyan, H. F. Taylor, W. Matous, T. Ottinger, and R. R. Neugaonkar, "Comparison of photorefractive damage effects in $LiNbO_3$, $LiTaO_3$, and $Ba_{1-x}Sr_xTi_yNb_{2-y}O_6$ optical waveguides at 488 nm wavelength", *Applied Physics Letters* **71**, 3051–3053 (1997).

[1.16] D. N. Nikogosyan, *Nonlinear Optical Crystals: A Complete Survey* (Springer, 2005), pp. 35–54, 185–190.

[1.17] M. Schall, H. Helm, and S. R. Keiding, "Far infrared properties of electro-optic crystals measured by THz time-domain spectroscopy", *International Journal of Infrared and Millimeter Waves* **20**, 595–604 (1999).

[1.18] E. D. Palik, *Handbook of Optical Constants of Solids* (Academic, 1998), pp. 777–805.

[1.19] S. S. Sussman, "Tunable light scattering from transverse optical modes in lithium niobate", Report No. 1851, Microwave Laboratory, Stanford University, Stanford, California,

1970).

[1.20] I. P. Kaminov and W. D. Johnson, Jr., "Quantitative determination of sources of the electro-optic effect in $LiNbO_3$ and $LiTaO_3$", *Physical Review* **160**, 519–522 (1967).

[1.21] R. Chen, G. Sun, G. Xu, Y. J. Ding, and I. B. Zotova, "Generation of high-frequency terahertz waves in periodically poled $LiNbO_3$ based on backward parametric interaction", *Applied Physics Letters* **101**, 111101 (2012).

[1.22] X. Lin, L. Wang, and Y. J. Ding, "Efficient generation of farinfrared radiation in the vicinity of polariton resonance of lithium niobate", *Optics Letters* **37**, 3687–3689 (2012).

[1.23] W. G. Spitzer and D. A. Kleinmann, "Infrared lattice bands of quartz," *Physical Review* **121**, 1324–1335 (1961).

[1.24] Y. J. Ding, "Efficient generation of far-infrared radiation from a periodically poled $LiNbO_3$ waveguide based on surface-emitting geometry", *Journal of the Optical Society of America B* **28**, 977 (2011).

[1.25] Y. H. Avetisyan, “Terahertz-wave surface-emitted difference-frequency generation without quasi-phase-matching technique”, *Optics Letters* **35**, 2508 (2010).

[2.1] U. Mishra, P. Parikh, and Y. Wu, “AlGaN/GaN HEMTs—An Overview of Device Operation and Applications”, Proceedings of the of IEEE **90**, 1022 (2012).

[2.2] H. Morkoc, *Nitride Semiconductors and Devices*, Springer, Heidelberg, 1999.

[2.3] K. T. Tsen, D. K. Ferry, A. Botchkarev, B. Sverdlov, A. Salvador, and H. Morkoc, “Direct measurements of electron-longitudinal optical phonon scattering rates in wurtzite GaN”, Applied Physics Letters **71**, 1852 (1997).

[2.4] H. Ye, G. W. Wicks, and P. M. Fauchet, “Hot electron relaxation time in GaN”, Applied Physics Letters **74**, 711 (1999).

[2.5] K. T. Tsen, D. K. Ferry, A. Botchkarev, B. Sverdlov, A. Salvador, and H. Morkoc, “Time-resolved Raman studies of the decay of the longitudinal optical phonons in wurtzite GaN”, Applied Physics Letters **72**, 2132 (1998).

[2.6] B. K, Ridley, “The LO phonon lifetime in GaN”, Journal of Physics: Condensed Matter **8**, L511 (1996).

[2.7] K. Wang, J. Simon, N. Goel and D. Jena, “Optical study of hot electron transport in GaN: Signatures of the hot-phonon effect”, Applied Physics Letters **88**, 022103 (2006).

[2.8] J. B. Khurgin, Y. J. Ding, and D. Jena, “Hot phonon effect on electron velocity saturation in GaN: A second look”, Applied Physics Letters **91**, 252104 (2007).

[2.9] R. Loudon, "Theory of the First-Order Raman Effect in Crystals", Proceedings of the Royal Society of London A **275**, 218 (1963).

[2.10] A. Link, K. Bitzer, W. Limmer, R. Sauer, C. Kirchner, V. Schwegler, M. Kamp, D. G. Ebling, and K. W. Benz, "Temperature dependence of the E_2 and A_1 (LO) phonons in GaN and AlN", Journal of Applied Physics **86**, 6256 (1999).

[2.11] S. Tripathy, G. Xu, X. Mu, Y. J. Ding, K. Wang, Y. Cao, D. Jena, and J. B. Khurgin, "Evidence of hot electrons generated from an AlN/GaN high electron mobility transistor", Applied Physics Letters **92**, 013513 (2008).

[2.12] S. Tripathy, G. Xu, X. Mu, Y. J. Ding, K. Wang, Y. Cao, D. Jena, and J. B. Khurgin, "Stokes and anti-Stokes resonant Raman scatterings from biased GaN/AlN heterostructure", Applied Physics Letters **93**, 051912 (2008).

[2.13] P. Perlin, C. Jauberthie-Carillon, J. P. Itie, A. San Miguel, I. Grzegory, and A. Polian, "Raman scattering and x-ray-absorption spectroscopy in gallium nitride under high pressure", Physical Review B **45**, 83 (1992).

[2.14] M. Leszczynski, T. Suski, H. Teisseyre, P. Perlin, I. Grzegory, J. Jun, S. Porowski, and T. D. Moustakas, "Thermal expansion of gallium nitride", Journal of Applied Physics **76**, 4909 (1994).

[2.15] J. B. Khurgin, D. Jena, and Y. J. Ding, "Isotope disorder of phonons in GaN and its beneficial effect on high power field effect transistors", Applied Physics Letters **93**, 032110 (2008).

[3.1] S. Chu, C. Cohen-Tannoudji and W. D. Philips, Nobel Prize in Physics 1997 for development of methods to cool and trap atoms with laser light.

[3.2] E. A. Cornell, W. Ketterle and C. E. Weiman, Nobel Prize in Physics 2001 for the achievement of Bose-Einstein condensation in dilute gases of alkali atoms, and for early fundamental studies of the properties of the condensates.

[3.3] P. Z. Pringsheim, "Zwei Bemerkungen über den Unterschied von Lumineszenz-und Temperaturstrahlung", Zeitschrift für Physik A **57**, 739 (1929).

[3.4] M. Sheik-Bahae and R. I. Epstein, "Laser cooling of solids", Laser & Photon. Rev. **3**, 67 (2009).

[3.5] S. Vavilov, "Some Remarks on the Stokes Law", Journal of Physics USSR **9**, 68 (1945).

[3.6] S, Vavilov, "Photoluminescence and Thermodynamics," Journal of Physics USSR **10**, 499 (1946).

[3.7] L. Landau, "On the Thermodynamics of Photoluminescence", Journal of Physics USSR **10**, 503 (1946).

[3.8] R. I. Epstein, M. I. Buchwald, B. C. Edwards, T. R. Gosnell and C. E. Mungan, "Observation of Laser-Induced Fluorescent Cooling of a Solid", Nature **377**, 500 (1995).

[3.9] D. V. Seletskiy, S. D. Melgaard, S. Bigotta, A. Di Lieto, M.Tonelli and M. Sheik-Bahae, "Laser Cooling of Solids to Cryogenic Temperatures", Nature Photonics **4**, 161 (2010).

[3.10] M. Sheik-Bahae and R. I. Epstein, “Can laser light cool semiconductors”, Physical Review Letter **92**, 247403 (2004).

[3.11] G. Rupper, N. H. Kwong, and R. Binder, “Large excitonic enhancement of optical refrigeration in semiconductors”, Physical Review Letter **97**, 117401 (2006).

[3.12] G. Rupper, N. H. Kwong, and R. Binder, “Optical refrigeration of GaAs: theoretical study”, Physical Review B **76**, 245203 (2007).

[3.13] L. A. Rivlin and A. Zadernovsky, “Laser cooling of semiconductors”, Optics Communications. **139**, 219 (1997).

[3.14] J. B. Khurgin, “Surface plasmon-assisted laser cooling of solids”, Physical Review Letter **98**, 177401 (2007).

[3.15] J. B. Khurgin, “Role of bandtail states in laser cooling of semiconductors”, Physical Review B **77**, 235206 (2008).

[3.16] J. B. Khurgin, “Band gap engineering for laser cooling of semiconductors”, Journal of Applied Physics **100**, 113116 (2006).

[3.17] S. Eshlaghi, W. Worthoff, A. D. Wieck and D. Suter, “Luminescence upconversion in GaAs quantum wells”, Physical Review B **77**, 245317 (2008).

[3.18] B. Imangholi, M. P. Hasselbeck, M. Sheik-Bahae, R. I. Epstein and S. Kurtz, “Effects of epitaxial lift-off on interface recombination and laser cooling in GaInP/GaAs heterostructures”, Applied Physics Lett. **86**, 081104 (2005).

[3.19] H. Gauck, T. H. Gfroerer, M. J. Renn, E. A. Cornell and K. A. Bertness, "External radiative quantum efficiency of 96% from a GaAs/GaInP heterostructure", Applied Physics A **64**, 143 (1997).

[3.20] J. Zhang, D. Li, R. Chen and Q. Xiong, "Laser cooling of a semiconductor by 40 kelvin", Nature **493**, 504 (2013).

[3.21] Y. P. Rakovich J. F. Donegan, M. I. Vasilevskiy and A. L. Rogach, Physica Status Solidi A **206**, 2497 (2009).

[3.22] S. Adachi, P. Capper, S. Kasap and A. Willoughby, *Properties of Semiconductor Alloys: Group-IV, III-V and II-VI Semiconductors*, pp 130 (Wiley 2009).

[3.23] Y.-F. Wu, A. Saxler, M. Moore, R. P. Smith, S. T. Sheppard, P. M. Chavarkar, T. Wisleder, U. K. Mishra and P. Parikh, "30-W/mm GaN HEMTs by Field Plate Optimization", IEEE Electronics Device Letter **25**, 117 (2004).

[3.24] F. A. Ponce and D. P. Bour, "Nitride-based semiconductors for blue and green light-emitting devices", Nature **386**, 351 (1997).

[3.25] C. F. Li, Y. S. Huang, L. Malikova, and F. H. Pollak, "Temperature dependence of the energies and broadening parameters of the interband excitonic transitions in wurtzite GaN", Physical Review B **55**, 9521 (1997).

[3.26] Urbach, F. "The Long-Wavelength Edge of Photographic Sensitivity and of the Electronic Absorption of Solids", Physical Review **92**, 1324 (1953).

[3.27] P. P. Paskov, P. O. Holtz, B. Monemar, J. M. Garcia, W. V. Schoenfeld and P. M. Petroff, “Photoluminescence up-conversion in InAs/GaAs self-assembled quantum dots”, Applied Physics Letter **77**, 812 (2000).

[3.28] C. K. Sun, J. C. Liang, J. C. Wang, F. J. Kao, S. Keller, M. P. Mack, U. Mishra and S. P. DenBaars, “Two-photon absorption study of GaN”, Applied Physics Letter **76**, 439 (2000).

Vita

Ruolin Chen was born on July 13, 1988 in Lanzhou, Gansu, China. He moved to Beijing, China with his family in 2003. In 2010, he received his Bachelor of Science degree in the major of Physics from Fudan University (Shanghai, China). After he graduated from Fudan University, he joined Department of Electrical and Computer Engineering of Lehigh University as a PhD student, in the major Electrical Engineering. During his PhD study, his research has been focused on nonlinear optics and semiconductor photonics, specifically, terahertz generation on nonlinear crystals, and photoluminescence and raman spectroscopy on GaN based materials and devices. To date, he has authored and coauthored 18 journal and conference publications. Apart from his academic study, he was also actively involved in student chapter activities such as SPIE, OSA, and IEEE Photonics Society. He served as the President of IEEE Photonics Society of Lehigh University Student Chapter from 2014 to 2015. He also actively participated in public speaking in the Toastmasters International. He served as the president of Toastmasters at Lehigh chapter for 3 months in the beginning of 2015.

Ruolin Chen

8 Duh Dr Apt 321 ▪ Bethlehem ▪ PA 18015 ▪ (484)602-3050
nic.rolling@gmail.com

EDUCATION

- **Lehigh University, Bethlehem, PA 18015, United States** 08/2010 – 09/2015
  Ph.D. Candidate in Electrical Engineering, Department of Electrical and Computer Engineering
  - Cumulative GPA: 3.95/4

- **Fudan University, Shanghai, China** 09/2006 – 07/2010
  Bachelor of Science in Physics, Department of Physics
  - Cumulative GPA: Major 3.79/4 Overall 3.20/4

RESEARCH EXPERIENCE

Lehigh University, Bethlehem, PA, USA 08/2010 – 09/2015
Research Assistant *in Electrical Engineering, Department of ECE*

- **Raman Spectroscopy study on GaN based materials and Devices**
  - Determined phonon temperature of GaN based high electron mobility transistor (HEMT) by ratio of stokes and anti-stokes Raman signal intensity, and by stokes frequency shifting
  - Reduced hot phonon temperature by using isotope GaN to fabricate HEMT
  - Investigated optical refrigeration based on GaN material by up-conversion
  - Calculated and set up laser sources by nonlinear process like SHG, SFG, DFG, OPO, OPA using commercial nonlinear crystals including BBO, KTP, $LiNbO_3$

- **Terahertz (THz) Generation on $LiNbO_3$ and $LiTaO_3$**
  - Calculated and performed backward THz generation based on optical rectification on periodically-ploed $LiNbO_3$ and $LiTaO_3$
  - Explored polariton resonance for enhancing THz generation, discovered beat phonon frequency rooting from lattice anharmonicity
  - Set up THz spectrometer using rotating stage, grating, parabolic mirrors and bolometer, programed spectrometer controlling console using Labview
  - Laser Oscillators and Amplifiers alignment and optimization: Mira 900, RegA 9000, OPO, OPA, Verdi 5, Verdi 10

- **Other Projects**
  - Photoluminiscence study on III-Nitride materials including InN, GaN, AlN and BN
  - GaN/AlGaN waveguide structure for optical parametric down conversion in transverse

geometry: design and calculation

AWARDS

- Lehigh University, **Rossin Doctoral Fellowship** (25 of all above 3rd year engineering students) — 2014 – 2015
- Lehigh University, **Sherman Fairchild Fellowship** (Outstanding students in semiconductor research) — 2014 – 2015
- Lehigh University, **Packard Fellowship** — 2013 – 2014
- Lehigh University, **Dean's Doctoral Assistanship** — 2010 – 2011
- Fudan University, **National Scholarship** (2% in all Fudan Students) — 2008 - 2009
- Fudan University, **People's Scholarship** — 2006 – 2008, 2009 – 2010

PROFESSIONAL AFFILIATION

- **President,** IEEE Photonics Society Student Chapter at Lehigh — 2014 - 2015
- **Student Member,** Institute of Electrical and Electronics Engineers (IEEE) — 2010 - Present
- **Member,** IEEE Photonics Society — 2011 – Present
- **Member,** Toastmasters International — 2014 - Present

REFERRED JOURNAL PUBLICATIONS

1. **R. Chen**, G. Xu, G. Sun, and Y. J. Ding, "Investigation of Backward THz Generation in Periodically Poled Stoichiometric $LiTaO_3$", J. Opt. Soc. Am. B. **31**, 3097 (2014).
2. **R. Chen**, G. Sun, G. Xu, Y. J. Ding, and I. Zotova, "Generation of high-frequency terahertz waves in periodically poled $LiNbO_3$ based on backward parametric interaction", Appl. Phys. Lett. **101**, 111101 (2012).
3. **R. Chen**, G. Sun, X. Lin, and Y. J. Ding, "Efficient generation of Record-Short and Record-Long Wavelengths Based on Backward and Forward Parametric Interaction in Lithum Niobate", in Proc. of SPIE Vol. 8623, 862317, March 2013.

4. G. Sun**, R. Chen**, Y. J. Ding, and J. B. Khurgin, "Upconversion Due to Optical-phonon-assisted Anti-stokes Photoluminescence in Bulk GaN", ACS Photonics, just accepted, DOI: 10.1021/acsphotonics.5b0015.

5. G. Sun, **R. Chen**, Y. J. Ding, H. Nguyen, and Z. Mi, "InGaN/GaN Dot-in-a-Wire: Ultimate Terahertz Nanostructure", Laser Photonics Rev. **9**, 105 (2015).

6. G. Sun, D. Li, **R. Chen**, and Y. J. Ding, "Transversely Pumped Spontaneous Parametric Fluorescence in GaN/AlGaN Waveguide", submitted.

7. G. Sun, **R. Chen**, Y. J. Ding, H. Zhao, G. Liu, J. Zhang, and N. Tansu, "Strikingly Different Behaviors of Photoluminescence and Terahertz Generation in InGaN/GaN Quantum Wells", IEEE J. Sel. Topics Quantum Electron. **19**, 8400106 (2013).

CONFERENCE PROCEEDINGS

1. **R. Chen,** G. Sun, Y. J. Ding, H. P. T. Nguyen, and Z. Mi, "Photoluminescence Upconversion Study of GaN Nanowires: Potential for Optical Refrigeration", in Proc. of CLEO:2015, San Jose, CA, USA, May 2015.

2. **R. Chen**, G. Sun, Y. J. Ding, and J. B. Khurgin, "Investigation of Hot Photons in GaN/AlN High Electron Mobility Transistor Based on Stokes Raman Scattering", in Proc. of CLEO:2014, San Jose, CA, USA, June 2014.

3. **R. Chen**, G. Xu, G. Sun, and Y. J. Ding, "Nonlinear Mixing of Transverse-Optical Phonon Frequencies through Strong Anharmonicity of $LiTaO_3$: Enhancing THz Generation", in Proc. of CLEO:2013, San Jose, CA, USA, June 2013.

4. G. Sun, **R. Chen**, Y. J. Ding, "Laser Cooling Based on Nitride Structures", Invited Talk, in Proc. of IPCon.2013 MH1.2, Bellevue, WA, USA, September 2013.

5. G. Sun, **R. Chen**, and Y. J. Ding, "Phonon-assisted Bandtail Anti-Stokes Photoluminescence of GaN: Novel Mechanism for Laser Cooling", in Proc. of CLEO:2013 QTu1E.2, San Jose, CA, USA, June 2013.

6. G. Sun, **R. Chen**, P. Zhao, Y. J. Ding, H. Nguyen, and Z. Mi, "Enhanced Terahertz Generation from InGaN/GaN Dot-in-a-Wire Light Emitting Diodes", in Proc. of CLEO:2013 JTh2A.57, San Jose, CA, USA, June 2013.

7. G. Sun, **R. Chen**, Y. J. Ding, H. Zhao, G. Liu, J. Zhang and N. Tansu, "Complementing Trends of Photoluminescence and Terahertz Intensities in Staggered InGaN Quantum Wells", in Proc. of CLEO:2013 JW2A.50, San Jose, CA, USA, June 2013.

8. G. Sun, **R. Chen**, P. Zhao, Y. J. Ding, H. Nguyen, and Z. Mi, "Efficient Terahertz Generation from InGaN/GaN Dot-in-a-Wire Nanostructure", in Proc. of CLEO:2012 CM2L.2, San Jose, CA, USA, May 2012.

9. G. Sun, **R. Chen**, Y. J. Ding, H. Zhao, G. Liu, J. Zhang, and N. Tansu, "Strikingly Different Behaviors of Photoluminescence Intensity and Terahertz Output Power versus Period of InGaN/GaN Quantum Wells", in Proc. of CLEO:2012 CTu2J.3, San Jose, CA, USA, May 2012.

10. G. Sun, D. Li, **R. Chen**, and Y. J. Ding, "Transverse Parametric Down Conversion in GaN/AlGaN Multilayer Waveguide", in Proc. of CLEO:2014 JTh2A.104, San Jose, CA, USA, June 2014.

11. Y. J. Ding, G. Sun, **R. Chen**, G. Xu, and I. Zotova, "Generation of Record-Short Wavelengths by Periodically-Poled $LiNbO_3$ Based on Backward Parametric Interaction", in Proc. of CLEO:2012 CTu1B.4, San Jose, CA, USA, May 2012.